

**Molecular Motion and Interactions in Solid  
Hydrogen Studied by High Resolution  
Infrared Spectroscopy**

**SONG, Yan**

A Thesis Submitted in Partial Fulfillment  
of the Requirements for the Degree of  
Doctor of Philosophy  
in  
Chemistry

The Chinese University of Hong Kong  
November 2009

UMI Number: 3436634

All rights reserved

**INFORMATION TO ALL USERS**

The quality of this reproduction is dependent upon the quality of the copy submitted.

In the unlikely event that the author did not send a complete manuscript and there are missing pages, these will be noted. Also, if material had to be removed, a note will indicate the deletion.



UMI 3436634

Copyright 2010 by ProQuest LLC.

All rights reserved. This edition of the work is protected against unauthorized copying under Title 17, United States Code.



ProQuest LLC  
789 East Eisenhower Parkway  
P.O. Box 1346  
Ann Arbor, MI 48106-1346

## **Thesis/Assessment Committee**

Professor Zhifeng Liu (Chair)

Professor Man-Chor Chan (Thesis Supervisor)

Professor Dominic Tak-Wah Chan (Committee Member)

Professor Shuiming Hu (External examiner)

Professor Allan Shi-Chung Cheung (External examiner)

## ABSTRACT

In this thesis, high resolution infrared spectrum of tetrahexacontapole (64-pole)-induced rovibrational  $W$  transition of solid parahydrogen (*para*-H<sub>2</sub>) was studied in samples containing ~0.05% of orthohydrogen (ortho-H<sub>2</sub>) using high resolution near infrared diode laser spectroscopy. The rovibrational  $W_1(0)$  transition ( $\nu = 1 \leftarrow 0, J = 6 \leftarrow 0$ ) has been observed at  $\sim 6441.73 \text{ cm}^{-1}$  with resolved triplet structure. These components were interpreted as the splitting of the  $M$  levels in the  $\nu = 1, J = 6$  state due to crystal field interaction. The corresponding crystal field parameters based on the model of localized exciton in the  $W_1(0)$  transition were determined. The good agreement of the corresponding parameters between the  $W_1(0)$  transition and the previous  $W_0(0)$  transition confirms the localization of the  $J = 6$  roton in both  $\nu = 0$  and 1 states for solid *para*-H<sub>2</sub>. In addition, the temperature dependence of the  $W_1(0)$  transition was studied in the temperature range of 2.7-8.0 K. The observed frequency shift has been ascribed to the change of isotropic intermolecular interactions as a result of molar volume change at different temperature.

In an attempt at studying tunneling motions in the solid *para*-H<sub>2</sub>, the infrared absorption spectrum of matrix-isolated ammonia molecules (NH<sub>3</sub>) has been studied using Fourier-transform infrared (FTIR) spectroscopy. The transitions of the ammonia molecule in the  $\nu_2$  fundamental band were observed to exhibit very different pattern compared to those observed in other matrix materials. A preliminary analysis of the observed spectrum was also discussed based on the effect of crystal annealing and nuclear spin conversion of NH<sub>3</sub>. Transitions have been assigned to

*ortho* and *para* species of  $\text{NH}_3$  based on their behavior in the presence of  $\text{O}_2$ . For a more definitive assignment, further experiments will be necessary.

Abstract of thesis entitled:

Molecular Motion and Interactions in Solid Hydrogen Studied by High Resolution Infrared Spectroscopy

Submitted by SONG Yan

for the degree of Doctor of Philosophy in Chemistry

at The Chinese University of Hong Kong in November 2009

## 中文摘要

本篇論文論述了利用高分辨近紅外半導體激光光譜儀，對固態仲氫（正氫含量約 0.05%）多極感應躍遷的研究。我們觀察到振轉躍遷  $W_1(0)$  ( $\nu = 1 \leftarrow 0, J = 6 \leftarrow 0$ )  $\sim 6441.73 \text{ cm}^{-1}$ ，且分辨出此振轉躍遷的三重態結構。運用晶體場相互作用理倫分析得出，該三重態結構是由  $\nu = 1, J = 6$  能級的  $M$  分裂所致。並且，利用最小二乘法擬合導出晶體場分裂參數與先前的轉動躍遷  $W_0(0)$  中所得之結果比較，可以推論  $J = 6$  的轉動能量是定域化的。此外，我們亦研究了振轉躍遷  $W_1(0)$  在 2.7-8.0 K 範圍的溫度效應。實驗觀察所得的頻率遷移可理解為固態仲氫在不同溫度下的摩爾體積改變而導致同向性相互作用改變的結果。

為研究分子在固態仲氫的隧道效應，我們利用傅立葉變換分光光譜儀，研究了摻雜在固態仲氫晶體中的氫分子的相關紅外吸收光譜。我們主要觀測了氫分子在  $\nu_2$  振動帶內的吸收躍遷，並發現所得吸收譜線與氫分子在其他晶體中的吸收譜線有很大差異。基於晶體退火效應和核自旋轉化作用，我們對實驗觀測的光譜進行了初步分析。根據氫分子在參雜氧分子的固態仲氫晶體中的行為，吸收躍遷可分別指認為仲氫和正氫的能級躍遷。然而，我們需要在未來進行更多的實驗以進一步指認躍遷。

## ACKNOWLEDGEMENTS

It is hard work to study on the approaches of molecular spectroscopy researches, so I would like to express my heartfelt gratitude and respect to those who have dedicated their energies to the studies in this field.

I owe particular thanks to my supervisor, Professor Man-Chor Chan, for helping me to clarify my thought and sharpen my thinking, for encouraging and instructing me to work out all the stages of my research, for assisting me to finish the writing of this thesis. Without his consistent and illuminating instruction, I have no idea how I can achieve this progress.

I would like to give my many thanks to my fellow members in the Laboratory of Laser Spectroscopy. I thank Lei Yan with whom I have worked closely and benefited deeply. He spent lots of time and effort on the whole process of this project without any complain. I thank Fangyuan Han for his friendship and invaluable help when I face frustrations. And also, I thank Zhenwu Liao and Mei Yang for making the lab an enjoyable place to come to each day.

On a personal note, my sincere thanks would go to my beloved parents for their affectionate considerations and great confidence in me all through these years. I received so much love from them and I will dedicate this thesis to them.

# TABLE OF CONTENTS

Thesis/Assessment Committee.....	ii
ABSTRACT.....	iii
中文摘要.....	v
ACKNOWLEDGEMENTS.....	vi
TABLE OF CONTENTS.....	vii
LIST OF FIGURES.....	ix
LIST OF TABLES.....	xi
CHAPTER I. Introduction.....	1
CHAPTER II. Theoretical Background.....	8
II.1. Symmetry Properties of H <sub>2</sub> Molecules.....	8
II.2. Nuclear Spin Modifications of H <sub>2</sub> Molecules.....	11
II.3. Molecular Symmetry in Solid H <sub>2</sub> .....	12
II.4. Multipole Moment and Polarizability.....	14
II.5. Long-range Intermolecular Interactions.....	16
CHAPTER III. Experimental Details.....	22
III.1. Gas Handling System.....	22
III.1.1. Ortho/para hydrogen converter.....	22
III.1.2. Gas mixing for matrix spectroscopy.....	27
III.1.3. Cryostat and sample holders.....	28
III.1.4. Solid sample preparation.....	30
III.2. Spectrometers.....	31

III.2.1. Diode laser spectrometer .....	31
III.2.2. Fourier-transform infrared (FTIR) spectrometer .....	34
CHAPTER IV. Tetrahexacontapole-induced Rovibrational <i>W</i> Transition of Solid Parahydrogen.....	39
IV.1. Background .....	39
IV.2. Theoretical Aspects .....	41
IV.2.1. Crystal field splitting .....	41
IV.2.2. Selection Rules and Relative Intensities .....	45
IV.2.3. Thermal effects.....	50
IV.3. Results.....	52
IV.3.1. Absorption spectrum .....	52
IV.3.2. Temperature effect .....	58
IV.4. Discussion .....	64
CHAPTER V. Spectroscopic Study of Ammonia in Parahydrogen Matrix..	66
V.1. Introduction.....	66
V.2. Theoretical Aspects .....	69
V.2.1. Group theoretical considerations.....	69
V.2.2. Nuclear spin modifications .....	77
V.3. Observation and Preliminary Analysis .....	78
V.4. Discussion .....	86
REFERENCE .....	87

## LIST OF FIGURES

FIGURE 1	For the hexagonal close-packed ( <i>hcp</i> ) structure.....	3
FIGURE 2	The standard set of variables for a pair of homonuclear diatomic molecules.....	18
FIGURE 3.	The vacuum system for the <i>para</i> -H <sub>2</sub> crystal preparation.....	23
FIGURE 4.	Schematic diagram of the normal H <sub>2</sub> to <i>para</i> -H <sub>2</sub> converter.....	25
FIGURE 5.	Liquid helium Dewar that accommodates the samples. ....	29
FIGURE 6.	Schematic diagram of the experimental setup for near infrared diode laser spectrometer .....	32
FIGURE 7	Schematic diagram of Michelson interferometer.....	35
FIGURE 8	Schematic diagram of the experimental setup for Bruker Vertex FTIR spectrometer .....	38
FIGURE 9	Crystal structure of an excited H <sub>2</sub> molecule ( $\nu = 1, J = 6$ ) in the <i>hcp</i> crystal environment consisting of the ground state hydrogen molecules ( $\nu = 0, J = 0$ ).....	42
FIGURE 10	Schematic of energy levels with crystal field splitting for the $W_1(0)$ transitions of solid hydrogen. ....	48
FIGURE 11	Overview of FTIR spectrum of ~99.95% solid <i>para</i> -H <sub>2</sub> samples at 0.2 cm <sup>-1</sup> resolution.. ..	53
FIGURE 12	Laser polarization dependence of the $W_1(0)$ transition of solid <i>para</i> -H <sub>2</sub> . ....	54
FIGURE 13	Observed temperature dependence of the $W_1(0)$ transition of solid <i>para</i> -H <sub>2</sub> .. ..	60

FIGURE 14	Frequency shift of the $W_1(0)$ transition of solid <i>para</i> -H <sub>2</sub> as a function of temperature. ....	61
FIGURE 15	Angle-independent transition frequency $\nu_0$ of the $W_1(0)$ transition of solid <i>para</i> -H <sub>2</sub> as a function of temperature. ....	63
FIGURE 16	Schematic representation of the two structures for ammonia. ....	67
FIGURE 17	Crystal structure of an XY <sub>3</sub> molecule trapped in the <i>hcp</i> crystal of <i>para</i> -H <sub>2</sub> . ....	70
FIGURE 18	Infrared absorptions in the $\nu_2$ region of NH <sub>3</sub> isolated in solid <i>para</i> -H <sub>2</sub> with mole ratio of 9 ppm. ....	80
FIGURE 19	The growing process of absorption pattern in the $\nu_2$ region of sample with 9 ppm NH <sub>3</sub> in ~99.95% <i>para</i> -H <sub>2</sub> matrix. ....	82
FIGURE 20	The annealing process of absorption pattern in the $\nu_2$ region of sample with 9 ppm NH <sub>3</sub> in ~99.95% <i>para</i> -H <sub>2</sub> matrix. ....	83
FIGURE 21	Dependence of absorption pattern on additional paramagnetic impurity O <sub>2</sub> content in the $\nu_2$ region of samples with 9 ppm NH <sub>3</sub> in ~99.95% <i>para</i> -H <sub>2</sub> matrix. ....	84

## LIST OF TABLES

TABLE 1	The character table for molecular symmetry group of H <sub>2</sub> molecule ....	10
TABLE 2	Character table of extended group $G$ .....	46
TABLE 3	Classification of the rotational wavefunction in the group $G$ .....	47
TABLE 4	Observed frequencies of the $W_1(0)$ transition for different samples.....	56
TABLE 5	Observed relative changes of frequencies for the $M$ components of the $W_1(0)$ transition in solid sample (I) at different temperatures. ....	62
TABLE 6	Character table of group $G_{72}$ .....	73
TABLE 7	Values of the Euler angles $\{\chi\theta\phi\}$ corresponding to the symmetry operations of point group $D_{3h}$ . ....	75
TABLE 8	Symmetry classifications of the rotational wavefunctions $ JKM\rangle$ ( $J \leq 2$ ) in group $G_{72}$ .....	76
TABLE 9	Observed absorptions (cm <sup>-1</sup> ) in the $\nu_2$ region for the sample of NH <sub>3</sub> in solid parahydrogen, with preliminary assignments. ....	81

## CHAPTER I. Introduction

Study of intermolecular interactions and molecular motions in the condensed phases has been a challenge in molecular spectroscopy. Spectral transitions in the condensed phases are usually homogeneously and inhomogeneously broadened due to strong intermolecular interactions, formation of energy bands, and variation of micro environment, etc. In addition, molecular rotation and vibration may be quenched by the strong interactions in the condensed phases. As a result, transitions often exhibit spectral widths much broader than a few wavenumbers unless some special techniques are applied.<sup>1-5</sup> However, solid parahydrogen has been an exception in which high resolution spectroscopy has been fully exploited.

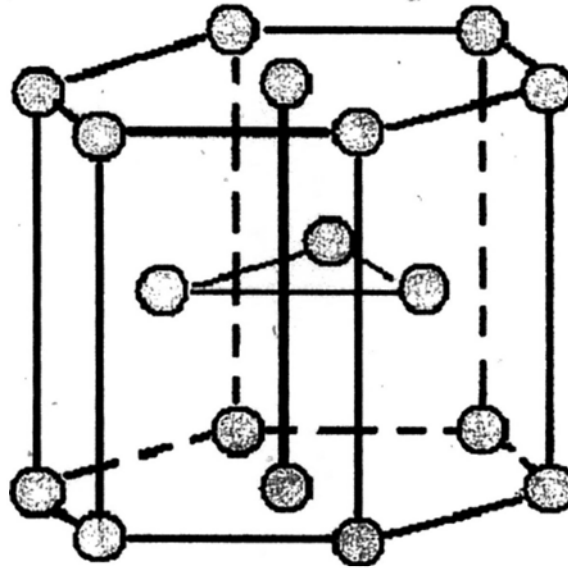
Although infrared transitions of  $H_2$  in the gas phase are dipole forbidden, the strong infrared absorption spectrum of solid hydrogen was first observed by Allin, Hare, and MacDonald in 1955 and hydrogen has been known to rotate nearly freely in condensed phase.<sup>6-7</sup> The sharp rovibrational transitions observed in the early years aroused interests from researchers to carry out extensive study. The results have been summarized in a number of review articles and manuscripts.<sup>18,36</sup> It has been known that  $H_2$  molecules in solid state retain their identity and thus solid  $H_2$  is dominated by quantum effects, which have been ascribed to the combination of small molecular mass, small molecular size, weak intermolecular interactions, and large intermolecular separation in solid state.

Spectral transitions in solid  $H_2$  can be as sharp as few MHz as first illustrated in the microwave spectrum of orthohydrogen impurity by Hardy, Berlinsky, Harris and their coworkers in the early 1980s.<sup>8-13</sup> The observation of the  $\Delta J = 6$  ( $W$ -branch)

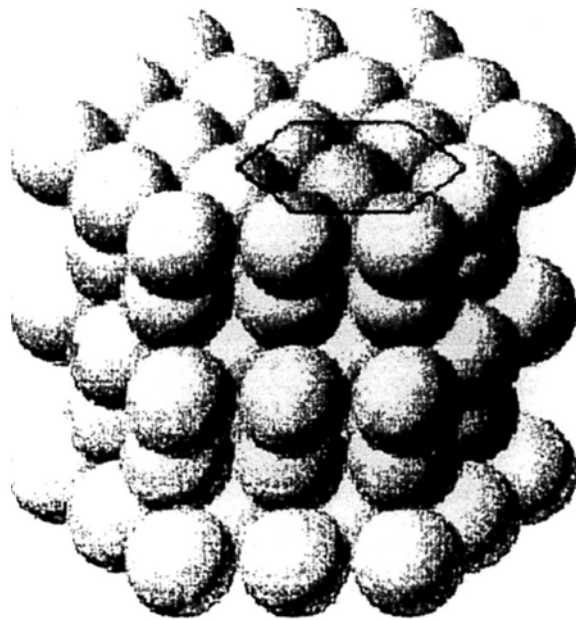
transitions of parahydrogen in the infrared region by Okumura, Chan and Oka in the late 1980s represented the first example that rovibrational transitions due to host crystal can be as sharp as  $\sim 100$  MHz.<sup>14-15</sup> This work has renewed the interest in pursuing high resolution laser spectroscopy in the system of solid hydrogen. Following the observation of the  $W$  transitions of *para*-H<sub>2</sub>, infrared spectra of a variety impurity species such as *ortho*-H<sub>2</sub>, *para*-D<sub>2</sub>, *ortho*-D<sub>2</sub>, CO, CH<sub>3</sub>, and CH<sub>4</sub> in *para*-H<sub>2</sub> crystal has been studied.<sup>15-22</sup> In addition, attempts at high resolution studies of ionic species in *para*-H<sub>2</sub> have also been reported.<sup>23-24</sup>

Hydrogen molecule, composed of two protons and two electrons, is one of the simplest and most fundamental molecules of all.<sup>30</sup> Due to the coupling of the two spin-1/2 protons, hydrogen molecules have two forms characterized by total nuclear spin  $I$ : Orthohydrogen (*ortho*-H<sub>2</sub>) with  $I = 1$  and parahydrogen (*para*-H<sub>2</sub>) with  $I = 0$ , respectively. At liquid helium temperature (4.2 K), only the two lowest rotational levels are populated due to the large rotational constant of hydrogen. The relaxation from the  $J = 1$  state to  $J = 0$  state involving change of total nuclear spin is a very slow process in the absence of catalysts. The details of nuclear spin and conversion between them will be discussed in the following chapters.

Most fundamental properties of solid hydrogen have been well summarized in a book by Souers<sup>26</sup> and in a review article by Silvera<sup>27</sup>. Here we just give a brief review of the properties related to our study. It has known that *para*-H<sub>2</sub> is a hexagonal closed packed (*hcp*) lattice as shown in FIGURE 1 when the solid is made from liquid to solid.<sup>27-28</sup> The *hcp* lattice is composed of a stacking of two hexagonal planes  $\alpha$  and  $\beta$ , with the nearest neighbor distance of 3.783 Å. Due to such large intermolecular separation compared with its small molecular size and very weak intermolecular interactions, individual *para*-H<sub>2</sub> molecules in the solid state



(a)



(b)

FIGURE 1 For the hexagonal close-packed (*hcp*) structure. (a) a reduced-sphere unit cell, and (b) an aggregate of many atoms.<sup>19</sup>

undergo nearly free rotation and vibration as shown in various spectroscopic studies.<sup>6,14,15,18,36</sup> The vibrational quantum number  $\nu$ , and the angular momentum quantum number  $J$  are good quantum numbers in the condensed phase as if in the gas phase. It should be noted that solid *para*-H<sub>2</sub> has very large amplitude of zero-point lattice vibration. The root mean square (rms) width of the single particle distribution function being about 20% of nearest-neighbor distance  $R_0$ .<sup>29</sup> As a result, hydrogen molecules are not sharply localized at lattice site even at  $T = 0$  K and thus solid H<sub>2</sub> has been considered as soft crystals. This phenomenon may be responsible for the fast diffusion of molecules and the extremely rich phases in the ultrahigh pressure regime for solid H<sub>2</sub>.

Despite the absence of permanent dipole moment for H<sub>2</sub> molecules, higher order multipole moments of H<sub>2</sub> play crucial roles in the spectroscopy of ultrahigh pressure gas and the condensed phase. First of all, the multipole moments of H<sub>2</sub> molecules can induce dipole moments on the nearby molecules as discussed in Chapter II. In the case of high pressure gas, the two interacting H<sub>2</sub> molecules act as a unit to absorb light that leads to a spectral transition. For instance, the quadrupole moment of molecule 1 induces a dipole moment on molecule 2 due to its polarizability. The induced dipole moment then interacts with the oscillating electric field associated with light to cause a spectral transition on molecule 1 or on both molecules 1 and 2, which have been known as single and double transitions, respectively. In the case of single transition, molecule 2 simply serves as an antenna for the absorption of light for molecule 1 even though molecule 2 does have the induced dipole moment. In the case of double transitions, both molecules change quantum states by absorbing *one photon*.

By applying the idea to the solid state and taking into account the point

symmetry of crystal environment, van Kranendonk established a rigorous theory to deal with the spectroscopic properties of solid hydrogen.<sup>30</sup> Dipole moments induced by multipole moments of different order are responsible for different infrared transitions according to the selection rules. The lowest three nonzero multipole moments of H<sub>2</sub> are quadrupole (4-pole), hexadecapole (16-pole), tetrahexacontapole (64-pole), which give rise to *Q* ( $\Delta J = 0$ ) and *S* ( $\Delta J = 2$ ) branches,<sup>6,31-32</sup> *U* ( $\Delta J = 4$ ) branch<sup>33-34</sup> and *W* ( $\Delta J = 6$ ) branch<sup>14</sup> single transitions, respectively. Compared to the usual multipole transitions, the multipole-induced transitions have the same selection rules but much stronger intensity that makes it observable in solid state. For instance, it can be shown that intensity ratio between a dipole allowed transition, a 64-pole transition and a 64-pole induced transitions is

$$I(\mu) : I(Q^6) : I(\mu_{md}^6) \sim 1 : 10^{-46} : 10^{-16} \quad (I - 1)$$

Recently, 128pole-induced transition with  $\Delta J = 8$  has been reported.<sup>35</sup> It is interesting that the perturbation of such weak interaction can be observed. The observed crystal field splitting of the rovibrational transitions in the crystal environment is due to anisotropic long range multipole-multipole interactions. The narrow linewidth in solid hydrogen allows the splitting to be resolved. This opens a new system for direct probing of the anisotropic intermolecular interactions using high resolution spectroscopy.

The remarkable work of the microwave spectroscopy of *ortho*-H<sub>2</sub> impurity in *para*-H<sub>2</sub> crystal held the promise of using *para*-H<sub>2</sub> as a host crystal for high resolution matrix spectroscopy.<sup>15,16,18,36</sup> Nevertheless, solid H<sub>2</sub> was not considered as a good matrix material because of its high vapor pressure at 4.2 K, its softness as a crystal, the difficulty in growing optically transparent crystal, and the extensive technical requirement for its handling. The preliminary studies of D<sub>2</sub><sup>17</sup>, HD<sup>37</sup>, CH<sub>4</sub><sup>19</sup>

and CO<sup>40</sup> in *para*-H<sub>2</sub> demonstrated narrow rotationally resolved infrared spectra can be obtained. Following these promising results, a number of molecules have been extensively studied including D<sub>2</sub>, HD, CH<sub>4</sub>, CO<sub>2</sub>, cyc-(H<sub>2</sub>O)<sub>6</sub>, HCl and DCl and so on.<sup>18,41-49</sup>

Following these studied, the advantage of using *para*-H<sub>2</sub> crystal as matrix material have been recognized and summarized.<sup>38</sup> Because of the large intermolecular distance and small molecular size, *para*-H<sub>2</sub> crystal provides a large space for a guest molecule to occupy a lattice site without seriously disturbing the crystal structure. Together with the weak intermolecular interaction, impurity molecules are allowed to undergo vibrational and rotational motion in the crystal with little hindrance. Furthermore, the lattice constant in solid parahydrogen is considerably larger than that in rare gas solids. Solid *para*-H<sub>2</sub> may thus be considered a soft medium (due to fast tunneling and swapping) so the relaxation of excited guest molecule may become much slower in *para*-H<sub>2</sub> matrix compared with rare gas matrices. In addition, the spherical charge density at the  $J = 0$  rotational state gives rise to the absence of permanent electric moment of any order that leading to slow relaxation and narrow homogeneous linewidth. As a result, the spectral linewidth of guest molecules in *para*-H<sub>2</sub> matrix is often sharp enough to resolve not only rotation structure and also fine structure resulting from crystal field splitting.

To date, spectroscopic studies on solid hydrogen have been focused on its optical properties, relaxation processes, and matrix properties. In this thesis, we report our experiments to study the crystal field splitting of the rovibrational  $W$  transition of *para*-H<sub>2</sub> crystal and our attempts at observing the inversion tunneling splitting of ammonia embedded in *para*-H<sub>2</sub> crystal. These studies represent the first step of our exploration of high resolution spectroscopy of solid H<sub>2</sub>. In Chapter II, a

brief theoretical background of the subject will be presented, followed by a description of the experimental setup in Chapter III. The results of the work for  $W$  transitions and  $\text{NH}_3$  will be discussed in Chapter IV and V, respectively.

## CHAPTER II. Theoretical Background

Hydrogen is one of the simplest molecular systems that have been extensively studied by theorists and experimentalists. Physical and chemical properties of  $H_2$  are well documented.<sup>51</sup> As a homonuclear diatomic molecule,  $H_2$  possesses no infrared spectrum as a result of the absence of dipole moment. The rovibrational transitions, however, can be observed due to the presence of intermolecular interactions for molecules under ultrahigh pressure (on the order of 100 GPa) and in the condensed phases. In this chapter, a brief review of the symmetry properties of  $H_2$  molecules and solid  $H_2$  will be presented in order to provide a theoretical background for spectroscopic purpose. In addition, the theory of intermolecular induced infrared transitions will also be outlined. For more detailed discussion of the subject, there are a number of excellent reviews available.<sup>30</sup>

### II.1. Symmetry Properties of $H_2$ Molecules

Symmetry (or invariance) is the most fundamental property of a molecular system. Symmetry consideration of a physical system provides qualitative yet rigorous arguments to classify its eigenstates, to visualize nonzero multipole moments and polarizability, as well as to predict the selection rules for transitions. Molecular symmetry group constructed based on molecular symmetry properties has been widely used in spectroscopy for this purpose. According to the geometric symmetry of molecules, molecular point group has long been used. Because of certain geometry is required for a molecule, the application of geometric symmetry

is limited to systems whose geometry is only slightly changed by molecular motion, *i.e.* semi-rigid molecules. By considering the symmetry properties of the molecular Hamiltonian under the permutation-inversion (PI) operations of identical particles, one can set up molecular symmetry group (MSG) that includes all *feasible* PI operations, *i.e.* operations can happen under the given experimental conditions. It can be shown that for semi-rigid molecules, each *feasible* PI operation corresponds to a finite rotation of the whole molecules in space. In addition, the MSG of a semi-rigid molecule is isomorphic to the corresponding molecular point group based on the symmetry. On the other hand, PI operations assume no geometry for the molecular system. PI group is therefore applicable in systems with or without definite geometry. This makes MSG a more rigorous and general approach to consider molecular symmetry.

The point group symmetry of H<sub>2</sub> molecule is well documented and will not be discussed here.<sup>56-59</sup> We will only consider the symmetry of H<sub>2</sub> molecule based on the idea of PI operations. It can be shown that hydrogen as homonuclear diatomic molecules belong to a molecular symmetry group with four PI operations:  $E$ ,  $(12)$ ,  $E^*$  and  $(12)^*$ , where  $E$  is the identity operation,  $(12)$  is the permutation of the two protons, and operations with asterisk indicate that an additional space inversion is followed. The corresponding character table is given in TABLE 1. The rovibrational levels of H<sub>2</sub> can therefore be classified according to the irreducible representations of the corresponding MSG.

According to the Pauli principle, the total wavefunctions of H<sub>2</sub> should belong to either  $\Sigma_u^+$  representation with positive parity or  $\Sigma_g^-$  representation with negative parity. By expressing the total wavefunctions as products of electronic (including spin), vibrational, rotational, and nuclear spin parts under the Born-Oppenheimer

TABLE 1 The character table for molecular symmetry group of H<sub>2</sub> molecule

$C_{2v}(M)$	$E$	$(12)$	$E^*$	$(12)^*$
$A_1$	1	1	1	1
$A_2$	1	1	-1	-1
$B_1$	1	-1	-1	1
$B_2$	1	-1	1	-1

approximation, one may classify the symmetry properties of each factor wave functions in the MSG. Since the ground state electronic wavefunctions and vibrational wavefunctions are totally symmetric in MSG, we only need to consider the symmetry of rotational and nuclear spin wavefunctions.

Molecular  $H_2$  is composed of two protons and two electrons. In the ground electronic state, the two electrons are in opposite spin and thus the overall electronic spin is zero. On the other hand, the two protons with spin  $\frac{1}{2}$  can combine to have nuclear spin 1 or 0, corresponding to spin parallel or anti-parallel, respectively. It can be shown that the nuclear spin wavefunction either belongs to  $\Sigma_g^+$  for total nuclear spin  $I = 1$  or  $\Sigma_u^+$  for total nuclear spin  $I = 0$ . In order to satisfy the requirement due to Pauli principle for total wavefunctions, rotational wavefunction with  $\Sigma_g^+$  symmetry (*i.e.* spherical harmonics with even rotational quantum number  $J$ ) should combine with  $I = 0$  nuclear spin while those with  $\Sigma_g^-$  symmetry (*i.e.* spherical harmonics with odd  $J$ ) should be combined with  $I = 1$  nuclear spin. For each  $I$  value, there are  $(2I+1)$   $M_I$  projections. As a result,  $I = 1$  species should be 3 times as abundant as  $I = 0$  species at room temperature.

## II.2. Nuclear Spin Modifications of $H_2$ Molecules

Since the conversion between different nuclear spin is facilitated by magnetic interaction that has positive parity, it is only operative between levels with the same parity. In the case of  $H_2$  molecules in the ground electron ground, however, rotational levels associated with different nuclear spin possess opposite parity arising from the factor  $(-1)^J$ . As a result, the conversion between  $I = 0$  and  $I = 1$  species of  $H_2$  is extremely slow due to the parity symmetry which is broken down only as a result of

the breakdown of Born-Oppenheimer approximation. In fact, it takes a few months for a sample of *para*-H<sub>2</sub> ( $I = 0$ ) gas to convert to normal H<sub>2</sub> gas. In other words, H<sub>2</sub> molecules with nuclear spins 1 and 0 can be considered as different molecules that are commonly referred to as nuclear spin modifications.

When a sample of H<sub>2</sub> equilibrated at room temperature (so-called normal H<sub>2</sub>) is cooled to  $T \rightarrow 0$  K, excessive amount of metastable  $I = 1$  species is obtained as a result of slow conversion between nuclear spin modifications. Nevertheless this conversion can be accelerated by the presence of paramagnetic materials that provide an inhomogeneous magnetic field. As discussed later, the parahydrogen used in our experiments was produced based on this principle.

### II.3. Molecular Symmetry in Solid H<sub>2</sub>

For molecules in the gas phase, the surrounding is isotropic so that the spatial orientation of molecules is irrelevant to the energies of rovibrational levels. On the other hand, molecules in the solid state are in an environment of finite symmetry. As a result, the rovibrational energies are perturbed by the anisotropic surroundings. In considering the symmetry of molecules in the solid state, as pointed out by *Miller and Decius*, both molecular symmetry and crystal symmetry should be taken into account in considering the symmetry of the whole system.<sup>60</sup> The appropriate symmetry group ( $G$ ) can be constructed by combining the pure permutation operations in the MSG ( $\bar{M}$ ) with pure rotational operations in the crystal point group ( $S$ ) and the permutation-inversion operations in  $\bar{M}$  with those involving reflection in  $S$ . These combinations are done to avoid changing only the crystal environment from right-handed system to left-handed system or vice versa. The appropriate combination is schematically shown below:

$$\overline{M} = \overline{M}(P) + \overline{M}(P^*) \text{ and } S = S(P) + S(P^*), \quad (\text{II - 2})$$

where  $P$  stands for a permutation and  $P^*$  stands for a permutation inversion. Then the appropriate extended group  $G$  consists of products of operations in  $S$  and  $\overline{M}$  expressed as:

$$G = \overline{M}(P) \otimes S(P) + \overline{M}(P^*) \otimes S(P^*) \quad (\text{II - 3})$$

In the following we will apply this approach to the system of solid hydrogen.

To construct the appropriate group, we consider a single  $\text{H}_2$  molecule in the hexagonal-close-packed (*hcp*) crystal environment. As discussed above, the MSG of  $\text{H}_2$  molecule is composed of four operations:

$$\overline{M} = \{ \overline{E}, \overline{(12)}, \overline{E}^*, \overline{(12)}^* \} \quad (\text{II - 4})$$

The point group of the *hcp* crystal is  $D_{3h}$  symmetry group composed of twelve operations:

$$S = \{ E, 2C_3, 3C_2, \sigma_h, 2S_3, 3\sigma_v \} \quad (\text{II - 5})$$

As a result, the group  $G$  is constructed as:

$$\begin{aligned} G &= \{ \overline{E}, \overline{(12)} \} \otimes \{ E, 2C_3, 3C_2 \} + \{ \overline{E}^*, \overline{(12)}^* \} \otimes \{ \sigma_h, 2S_3, 3\sigma_v \} \\ &= \{ \overline{E}E, 2\overline{E}C_3, 3\overline{E}C_2, \overline{(12)}E, 2\overline{(12)}C_3, 3\overline{(12)}C_2 \} \\ &\quad + \{ \overline{E}^*\sigma_h, 2\overline{E}^*S_3, 3\overline{E}^*\sigma_v, \overline{(12)}^*\sigma_h, 2\overline{(12)}^*S_3, 3\overline{(12)}^*\sigma_v \} \end{aligned} \quad (\text{II - 6})$$

The character table of group  $G$  can be constructed using standard procedure in group theory based on the character tables of  $S$  and  $\overline{M}$ . Once the character table of  $G$  is established, the rovibrational states of central  $\text{H}_2$  molecule can be classified accordingly.

If the central  $\text{H}_2$  molecule is replaced by a guest molecule (*i.e.*  $\text{O}_2$ ,  $\text{NH}_3$ ,  $\text{CO}$ , etc.) in the case of matrix isolated molecules, the symmetry group is constructed in the same fashion except that the  $M$  should be replaced by the MSG of the guest

molecule.

## II.4. Multipole Moment and Polarizability

The non-spherical charge distribution of  $H_2$  molecules leads the existence of multipole moments. According to electrostatic theory, the electric potential  $\Phi(\bar{R})$  at a distance  $\bar{R}$  produced by an arbitrary charges distribution (continuous or discrete source) can be expressed power series of  $R$ :

$$\Phi(\bar{R}) = \sum_{lm} Q_{lm} \frac{1}{R^{l+1}} C_{lm}^*(\theta, \phi) \quad (\text{II - 7})$$

where  $C_{lm}(\theta, \phi)$  is the spherical harmonic and  $Q_{lm}$  is defined the spherical component of the multipole moment of order  $l$  of the system. For discrete charge distribution, we have

$$Q_{lm} = \sum_i e_i r_i^l C_{lm}(\theta_i, \phi_i) \quad (\text{II - 8})$$

where  $r_i$  is the position of charge  $e_i$  measured from the origin of reference.  $Q_{lm}$  corresponds to  $l$  pairs of opposite charges positioned in certain arrangement in space. For the zeroth-order ( $l = 0$ ),  $Q_{00} = \sum_i e_i$  is the net charge (also known as monopole).

The first-order term  $Q_{1m} = \sum_i e_i r_i$  is denoted as the dipole moment and the second-, third-, etc. order terms are denoted as quadrupole moment, octupole moment, etc. Correspondingly, for continuous charge distribution with charge density  $\rho(\bar{r})$ , the multipole moment can be defined as:

$$Q_{lm} = \int \rho(\bar{r}) r^l C_{lm}(\theta, \phi) d\bar{r} \quad (\text{II - 9})$$

where  $d\bar{r} = r^2 \sin \theta \cdot dr d\theta d\phi$ .

The multipole moment  $Q_{lm}$  of a charge distribution has  $2l+1$  quantities, corresponding to  $m = l, l-1, \dots, -l$ . In the case of  $H_2$  molecules, an axially symmetric charge distribution requires only one independent component along the molecular axis for each non-vanishing multipole moment. In other words, in the molecular-fixed frame, all the components  $Q'_{lm}$  vanish except  $Q'_{l0}$  which is then called the multipole moment  $Q^{(l)}$

$$Q^{(l)} \equiv Q'_{l0} = \sum_i e_i r_i^l P_{lm}(\cos \theta'_i) \quad (\text{II - 10})$$

The value of  $Q_{lm}$  in a space-fixed frame is related to  $Q^{(l)}$  by

$$Q_{lm} = C_{lm}(\beta, \alpha) Q^{(l)} \quad (\text{II - 11})$$

where  $\beta, \alpha$  are the polar angles of the molecular axis in the space-fixed system.

Under the adiabatic approximation, the permanent multipole moment of rovibrational state  $\langle \nu J | Q^{(l)} | \nu J \rangle$  is evaluated from the first principles by

$$\langle \nu J | Q^{(l)} | \nu J \rangle = \int_0^{\infty} u_{\nu J}(r) Q^{(l)} u_{\nu J}(r) dr \quad (\text{II - 12})$$

where  $u_{\nu J}$  denotes the radial part of the rotation-vibrational wavefunction specified by quantum numbers  $\nu$  and  $J$ . It should be noted that the inversion center of  $H_2$  molecules requires permanent moments with odd  $l$  to be zero. The transition multipole moment between states  $u_{\nu J}$  and  $u_{\nu' J'}$  can be evaluated similarly,

$$\langle \nu J | Q^{(l)} | \nu' J' \rangle = \int_0^{\infty} u_{\nu J}(r) Q^{(l)} u_{\nu' J'}(r) dr \quad (\text{II - 13})$$

As discussed in the next section, the permanent and transition multipole moments of  $H_2$  are of fundamental importance in understanding the rovibrational spectroscopy of solid hydrogen.

In the presence of external electric field  $E$ , the charge distribute of molecules is

distorted to generate induced moments according to equation

$$\mu_i = \sum_j \alpha_{ji}(\bar{r}) E_j \quad (\text{II - 14})$$

where  $i$  and  $j$  indicate the Cartesian components of the corresponding vectors.  $\alpha_{ji}$  is defined as the components of the polarizability tensor, a second rank Cartesian tensor. For  $\text{H}_2$  molecules, the axial symmetry requires once again that there are only two nonzero independent components referred to the molecular-fixed frame, *i.e.* the one parallel ( $\alpha_{||}$ ) or perpendicular ( $\alpha_{\perp}$ ) to the molecular axis. It is obvious that

$$\alpha_{x'x'}(r) = \alpha_{y'y'}(r) = \alpha_{\perp}(r) \quad \text{and} \quad \alpha_{z'z'}(r) = \alpha_{||}(r) \quad (\text{II - 15})$$

More commonly, polarizability tensor is expressed in the form of isotropic polarizability  $\alpha(r) = \frac{1}{3}(\alpha_{xx} + \alpha_{yy} + \alpha_{zz}) = \frac{1}{3}(2\alpha_{\perp} + \alpha_{||})$  and the anisotropic polarizability  $\gamma(r) = (\alpha_{||} - \alpha_{\perp})$ . And also, polarizability tensor can be expressed in terms of spherical components as discussed by Van Kranendonk.<sup>30</sup>

Similar to the case of multipole moments, the components of polarizability tensor can also be evaluated theoretically according to standard procedure in quantum mechanics.

## II.5. Long-range Intermolecular Interactions

Intermolecular interactions play a crucial role in the rovibrational spectroscopy of solid parahydrogen. In this section, a brief overview of intermolecular interactions will be presented. More detailed discussion of the subject can be found elsewhere.<sup>30</sup>

The total energy of a system composed of two molecules separated by a finite distance  $R$  can be written in the form

$$E_{tot}(X, R) = E_{tot}(X, \infty) + V(X, R) = \varepsilon_0(r_1) + \varepsilon_0(r_2) + V(X, R) \quad (\text{II - 16})$$

where  $X = (r_1, r_2, \theta_1, \theta_2, \phi)$  represents the set of variables to describe the relative position between the two molecules as shown in FIGURE 2,  $r_1$  and  $r_2$  denote the nuclear coordinates for the molecule 1 and 2, respectively,  $\varepsilon_0(r_i)$  is the energy of an isolated molecule  $i$ , respectively. Since the extra contribution to the total energy arises from the interaction between the two molecules, the intermolecular pair potential is defined as

$$V(X, R) = E_{tot}(X, R) - \varepsilon_0(r_1) - \varepsilon_0(r_2) \quad (\text{II} - 17)$$

The pair energy  $V(X, R)$  vanishes when the two molecules are infinitely separated. Equation (II-16) indicates that intermolecular energy depends on the intermolecular separation and relative orientation as well as the internal coordinates of each individual molecule. In other words, the internal energy of the molecules themselves, *i.e.* vibrational and rotational energy, also contributes to the intermolecular pair potential of the system.

Since the intermolecular forces have an electromagnetic origin, the potential energy surface for a two-molecule system must have at least two contributions from the long-range attraction and the short-range repulsion corresponding to the large and small intermolecular separation  $R$ . The short-range repulsive part can be easily interpreted by large overlap of the electron clouds of the molecules at the short separation  $R$ . The electron density in this region thus reduces due to the Pauli Exclusion Principle and the positively charged nuclei of molecules are incompletely shielded from each other resulting in a Coulomb repulsive force on each other. The theoretical treatment of the short-range repulsive forces between molecules at small distances of separation can only be done using high level *ab initio* calculations similar to the case of chemical bonding. To date, there are various approaches to

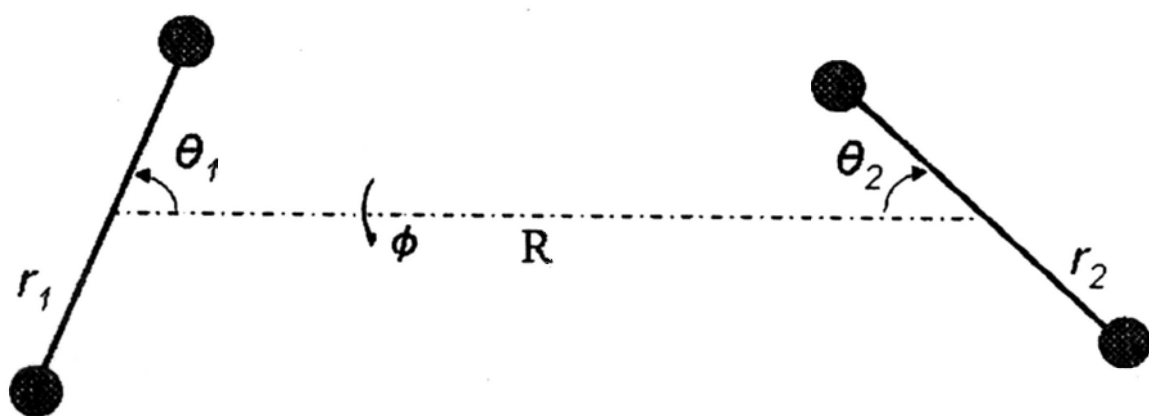


FIGURE 2 The standard set of variables for a pair of homonuclear diatomic molecules.

theoretically evaluate short-range repulsive forces. Conversely, the long-range attractive part of the intermolecular force, corresponding to the region with little overlap of electron clouds, arises from the interaction of one molecule with the multipole fields created by the other molecule.

The mathematical account of the long-range intermolecular interaction is rendered by perturbation theory. If the classical perturbation energy is  $V(X, R)$ , the change of the ground state energy of molecules is given by

$$\Delta E_{00} = \langle 00 | V(X, R) | 00 \rangle - \sum_{rs} \frac{|\langle rs | V(X, R) | 00 \rangle|^2}{E_{rs} - E_{00}} + \dots \quad (\text{II - 18})$$

where  $r$  and  $s$  is a set of quantum numbers representing the excited electronic energy for molecule 1 and 2, respectively and  $E_{rs} = \varepsilon_0(r_1) + \varepsilon_0(r_2)$ . The first term in the equation above corresponds to the interaction between permanent multipole moments of one molecule in the multipole fields of another molecule. Without significant distortion of the electron distribution, this permanent multipole-multipole interactions term gives rise to the first order correction in energy. On the other hand, the second term with either  $r = 0$  or  $s = 0$  corresponding to the polarization of one molecule by the permanent multipole fields of the other molecule. The multipole moments induced by polarization interact with the original field of permanent multipoles to give rise to an energy correction, which is known as the induction interactions. With both  $r$  and  $s \neq 0$ , the second term corresponds to interactions between momentarily fluctuating multipole fields of the two molecules. This interaction is known as the dispersion energy which is always present regardless of the nature of the pair of molecules involved. It is the dominant long-range attraction energy for molecules with no permanent electric dipoles. Both induction and dispersion interactions contributes to the second-order correction of energy.

The detailed form of  $V(X, R)$  can be understood based on classical electrostatic interactions. According to the expression of electric potential Equation (II-6) due to multipole moments, we can determine the corresponding electric field  $E = -\nabla\Phi$ . The spherical components  $E_\alpha$  of the field at a distance  $\bar{R} = (R, \Omega)$  from a multipole of order  $l$  are expressed as

$$E_\alpha(\bar{R}) = -\sum_m Q_{lm} \nabla_\alpha \frac{C_{lm}^*(\Omega)}{R^{l+1}} \quad (\text{II - 19})$$

where  $Q_{lm}$  is multipole moment given by Equation (II-10). Using the expression of the gradient formula,<sup>61</sup>  $E_\alpha$  can be rewritten as

$$E_\alpha(\bar{R}) = (-1)^\alpha [(l+1)(2l+1)]^{1/2} \sum_m Q_{lm} C(1, l, l+1; \alpha \bar{m}) \frac{C_{l+1, m-\alpha}^*(\Omega)}{R^{l+2}} \quad (\text{II - 20})$$

where  $C(1, l, l+1; \alpha \bar{m})$  is Clebsch-Gordan coefficient in which only the maximum value  $l' = l+1$  is allowed by the triangle condition  $\Delta(1ll')$ . The interaction energy between two multipoles of order  $l_1$  and  $l_2$  can be obtained by

$$V_{l_1 l_2} = \varepsilon_{l_1 l_2}(R) \sum_{mn} C(l_1, l_2, l_1 + l_2; mn) C_{l_1 m}(\Omega_1) C_{l_2 n}(\Omega_2) C_{l_1 + l_2, m+n}^*(\Omega_{12}) \quad (\text{II - 21})$$

where  $\varepsilon_{l_1 l_2}(R) = (-1)^{l_2} \left[ \frac{(2l_1 + 2l_2)!}{(2l_1)!(2l_2)!} \right]^{1/2} \frac{Q_{l_1} Q_{l_2}}{R^{l_1 + l_2 + 1}}$

By choosing the axis system with the  $z$  axis along  $\bar{R}_{12}$ , the interaction energy  $V_{l_1 l_2}$  can be simplified as

$$V_{l_1 l_2} = \varepsilon_{l_1 l_2}(R) \sum_m C(l_1, l_2, l_1 + l_2; m \bar{m}) C_{l_1 m}(\omega_1) C_{l_2 \bar{m}}(\omega_2) \quad (\text{II - 22})$$

In solid hydrogen molecules, the permanent quadrupole-quadrupole interaction is the most dominant first order energy correction between  $J = 1$  molecules, whereas the quadrupole-(induced dipole) and (induced dipole)-(induced dipole) are the most

dominant contribution between molecules with  $J = 0$ . This mathematic framework will be applied in dealing with the crystal field splitting of rovibrational energy.

## CHAPTER III. Experimental Details

A new experimental setup has been built from scratch to pursue the spectroscopic studies of solid parahydrogen. The system is composed of two major parts, namely the gas handling system for the production of solid parahydrogen crystals and the spectrometer system for recording the spectra. In this chapter, the details of these parts will be described.

### III.1. Gas Handling System

In order to build a gas system that can be accommodated to different experiments, we incorporated various components with different functionality. The overall schematic of the system is shown in FIGURE 3. In a typical run, normal hydrogen ( $n\text{-H}_2$ ) from commercial gas tank was first converted to *para*- $\text{H}_2$  gas in an inline ortho/*para* converter (C). The *para*-enriched  $\text{H}_2$  gas from the converter was then stored in a stainless steel vessel (A). For the W transition studies, the gas from the storage vessel was directly used whereas in the matrix studies the *para*- $\text{H}_2$  gas will be mixed with impurity gases in another stainless steel vessel (B). The solid sample was prepared by depositing the gas/mixture gas from vessel (B) to the sample holder (D) cooled at liquid He temperature. In the following sections, each part of the gas handling system will be discussed.

#### III.1.1. Ortho/*para* hydrogen converter

As mentioned in Chapter II, the ratio of *ortho*- $\text{H}_2$  to *para*- $\text{H}_2$  in normal hydrogen gas is 3:1 at room temperature. Due to almost identical physical properties

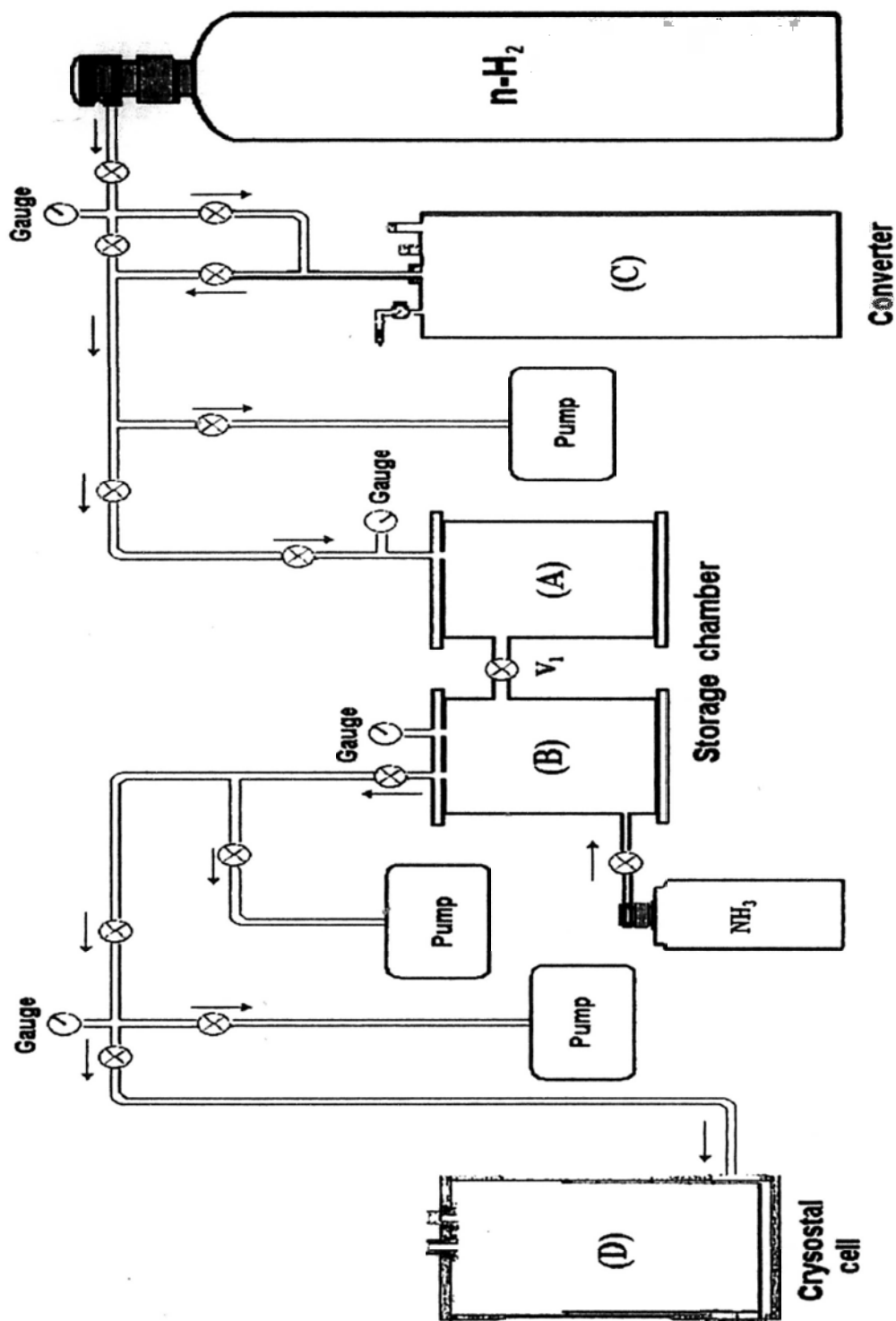


FIGURE 3. The vacuum system for the *para*- $\text{H}_2$  crystal preparation. The *para*-enriched  $\text{H}_2$  gas was converted from the normal  $\text{H}_2$  gas in the conversion (C) at 14~20 K, and then it was rushed into the storage chamber (A) and (B). After that, the *para*- $\text{H}_2$  crystal was grown in the cryostat cell (D) for study of spectroscopy. “⊗” denotes the vacuum valve used in experiments, *i.e.*  $V_1$ .

between the two species, the conversion from *ortho* to *para* hydrogen cannot be achieved simply by physical method, such as cryogenic distillation. However, the *ortho/para* conversion rate can be greatly increased by using a suitable catalyst (such as APPACHI catalyst) that provides an external inhomogeneous magnetic field around the absorbed hydrogen molecules.<sup>25</sup> Such a magnetic field can result in fast equilibrium between the *ortho*-H<sub>2</sub> and *para*-H<sub>2</sub> concentrations by controlling the temperature of the catalyst. Based on the design of Sibener and coworkers, an inline *ortho/para* converter filled with paramagnetic ferric oxide (Fe<sub>2</sub>O<sub>3</sub>) from C\*CHEM was built for our experiments to produce *para*-enriched H<sub>2</sub> gas from normal H<sub>2</sub> gas.<sup>62</sup>

The schematics of *ortho/para* converter is shown in FIGURE 4. A cylindrical stainless steel container with 5 cm in diameter and 8 cm in length was used to house the Fe<sub>2</sub>O<sub>3</sub> catalyst (in the form of fine powder in order to maximize its surface area for the adsorption of H<sub>2</sub> gas). Two concentric stainless steel tubes of diameters 3/8 and 1/8 inch with relief valves are connected to the container as the gas inlet and outlet lines, respectively. As shown in the figure, the outer tube was soldered on the top cover of the catalyst container while the inner tube fitted with gas filter at the bottom to prevent the catalyst powder from entering the vacuum system was positioned at the lower cover of the container. The temperature of catalyst container was monitored using two diode sensors (Lakeshore Cryotronics) installed on its top and bottom covers. The whole container system was kept in a custom-designed liquid helium Dewar (Cryofab, Inc.), cooled with liquid Helium. During conversion, the temperature of the converter was controlled by its distance from the liquid He level. The catalyst was initially activated by heating to a temperature range of 150 to 170 °C for a few hours while passing through hydrogen gas to remove impurity gas molecules adsorbed on the surface of the catalyst. After this process, the converter

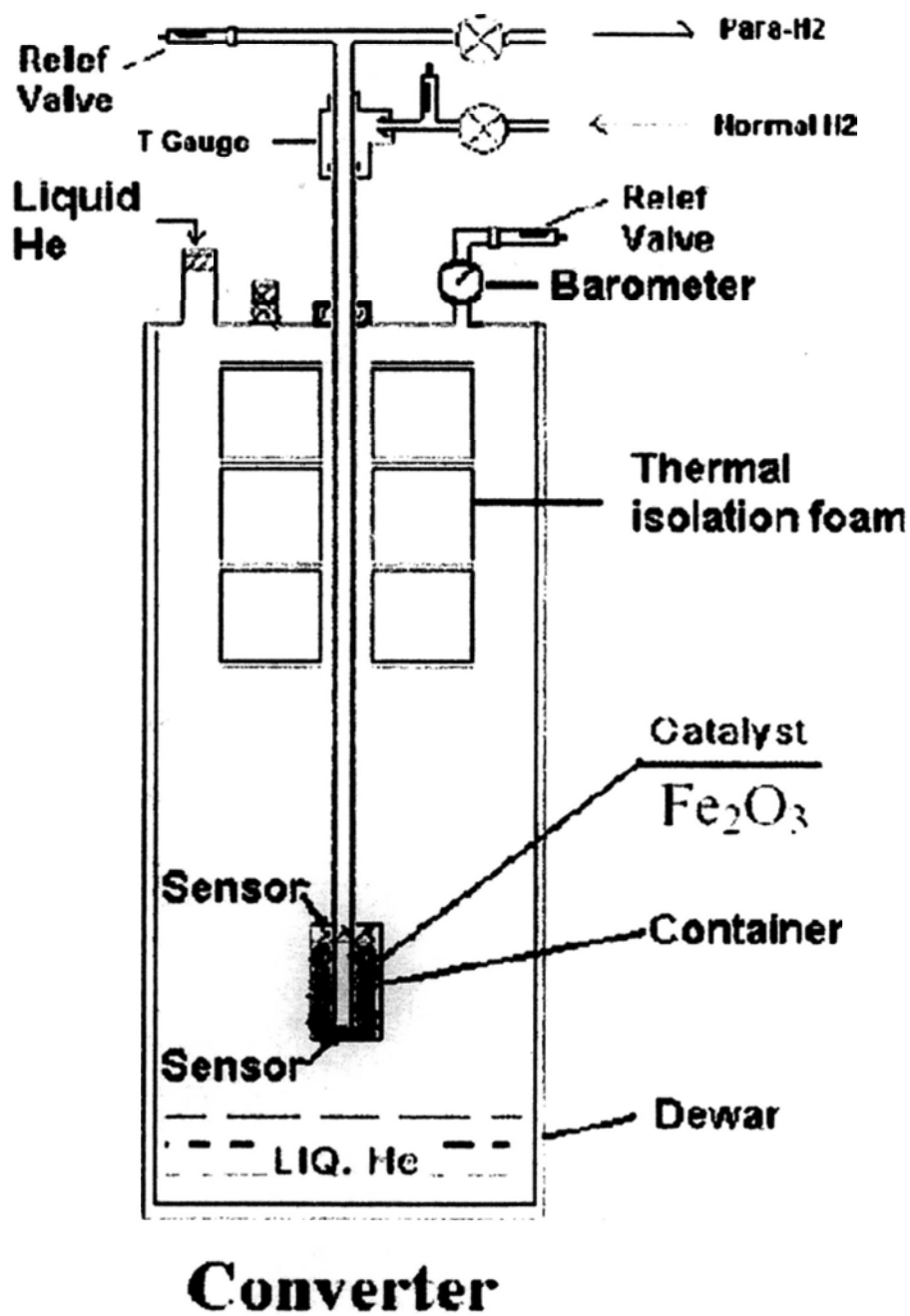


FIGURE 4. Schematic diagram of the normal H<sub>2</sub> to *para*-H<sub>2</sub> converter

was evacuated for 24 hours before used.

In the preparation of *para*-H<sub>2</sub> gas, the Dewar was filled about 1.5 inch liquid Helium while the container was raised above the liquid He level to reach a temperature of ~14 K. Normal H<sub>2</sub> gas was then slowly added into the container while maintaining the temperature at 14-16 K. In order to maximize the amount of adsorbed gas, temperature fluctuation of the container was kept as small as possible. After the adsorption of H<sub>2</sub> gas was essentially complete as shown by the constant temperature sensor reading, the gas input valve was closed and the container was held at about 14 K for at least one hour to let the adsorbed H<sub>2</sub> gas to reach thermal equilibrium in the presence of an inhomogeneous magnetic field. The efficiency of the conversion from *ortho* to *para* H<sub>2</sub> through catalysis is limited by the conversion temperature. In order to maximize the efficiency of conversion, the conversion temperature should be above the triple point to allow greater mobility of H<sub>2</sub> molecules. Since the equilibrium *ortho*-H<sub>2</sub> concentration varies from around 0.004% to 0.2% in the temperature range of 14 to 20 K, it is crucial to control the temperature in this range. To release the adsorbed gas after conversion, the container temperature (catalyst temperature) was raised to about 15 K (measured by the bottom sensor). The valve of output was opened to allow the flow *para*-enriched H<sub>2</sub> gas to the storage container. Special care should be taken in controlling the temperature at this stage to avoid back conversion between *para* and *ortho* species due to rapid increase of temperature. The typical *ortho*-H<sub>2</sub> content obtained following this procedure was about 0.05%.

The actual *ortho*-H<sub>2</sub> content was determined quantitatively from the experimental integrated intensities of the  $Q_1(1)$  transition based on the theoretical value of  $\tilde{\alpha}$  (in cm<sup>3</sup>/s) defined as

$$\tilde{\alpha} = \frac{c}{nL} \int \ln \left[ \frac{I_0(\nu)}{I(\nu)} \right] d\nu / \nu, \quad (\text{III - 1})$$

which is related to the common integrated absorption coefficient  $\alpha'$  (in  $\text{cm}^{-2}$ ) expressed as

$$\alpha' = \frac{1}{L} \int \ln \left[ \frac{I_0(\nu)}{I(\nu)} \right] d\nu. \quad (\text{III - 2})$$

by a factor of  $c/n$ . In these expression,  $n$  is the number density of molecules,  $c$  is the speed of light,  $L$  is the absorption path length,  $\nu$  is the frequency in  $\text{cm}^{-1}$ ,  $I_0(\nu)$  and  $I(\nu)$  are the intensity of incident and transmitted light, respectively. The number density of *ortho*- $\text{H}_2$  in the crystal of length  $L$  can then be determined from the experimental integrated intensity of  $Q_1(1)$  transition and the corresponding theoretical value of  $\tilde{\alpha} = 1.03 \times 10^{-15} \text{ cm}^3 / \text{s}$ .<sup>63</sup>

### III.1.2. Gas mixing for matrix spectroscopy

In pursuing spectroscopy of trace impurity molecules embedded in solid *para*- $\text{H}_2$  matrices, a pre-mixture of dopant gas (e.g. ammonia) and *para*-enriched  $\text{H}_2$  gas was prepared at room temperature. In order to isolate dopant molecules in *para*- $\text{H}_2$  matrix as much as possible, the typical dopant/ *para*- $\text{H}_2$  ratio is about  $10^{-5} \sim 10^{-6}$ . Gas mixture of any planned ratios was prepared using the two stainless steel vessels (A) and (B). The mixing procedure is described below. The two vessels were initially evacuated prior to experiments. Vessels (A) and (B) were then isolated by closing the valve ( $V_1$ ). Vessel (A) was then filled with freshly prepared *para*- $\text{H}_2$  gas to about 40 kPa as described above. Vessel (B) was then filled with dopant gas, whose pressure (in the range of 0.1~20 pa) was measured by a low-pressure membrane manometer shown in FIGURE 3. Parahydrogen gas from vessel (A) was then allowed to flow to vessel (B) by opening the valve ( $V_1$ ) until the desirable

pressure (on the order of 20 kPa as measured by a high-pressure membrane manometer) was reached. The gas mixture in vessel (B) was then ready for use in producing matrix samples. Due to the much higher pressure in vessel (A), the mixing was completed in seconds and the diffusion of dopant gas from (B) to (A) is expected to be minimal. This procedure effectively minimizes the error in calculating mixing ratio.

### **III.1.3. Cryostat and sample holders**

All the solid hydrogen samples were grown in a cryostat modified from a commercial liquid helium Dewar (Infrared Laboratories, HD-5). It is a double jacket type with a radiation shield heat-sunk to a liquid nitrogen tank enclosing the liquid-helium-temperature compartment. All the interior Dewar surfaces were covered with aluminum foil in order to provide additional shielding. The sample cells were mounted on the cold surface of the cryostat to maintain close to liquid He temperature for crystal growth and subsequent experiments. Two optical windows (CaF<sub>2</sub> or ZnSe) of 1 inch in diameter were sealed by o-ring and installed along the optical axis of the Dewar to allow the passage of infrared radiation. The schematic diagram of the Dewar is shown in FIGURE 5. The hold time of the Dewar is close to 30 hours to allow long-hour experiments.

Two different sample cells were used in the work presented here. In studying the W transition of *para*-H<sub>2</sub> crystal, a cylindrical sample cell made of OFHC copper with length of 3 cm and diameter of 15 mm was used. Both ends of the cell were sealed with sapphire windows of 22 mm in diameter using indium gaskets. A 1/16 inch O.D. thin wall stainless steel tube is soldered on the cell as gas inlet/outlet tube. It was then directed to the outside of the Dewar through vacuum feedthrough. A diode temperature sensor (Lakeshore Cryotronics 670-SD) was installed on the cell

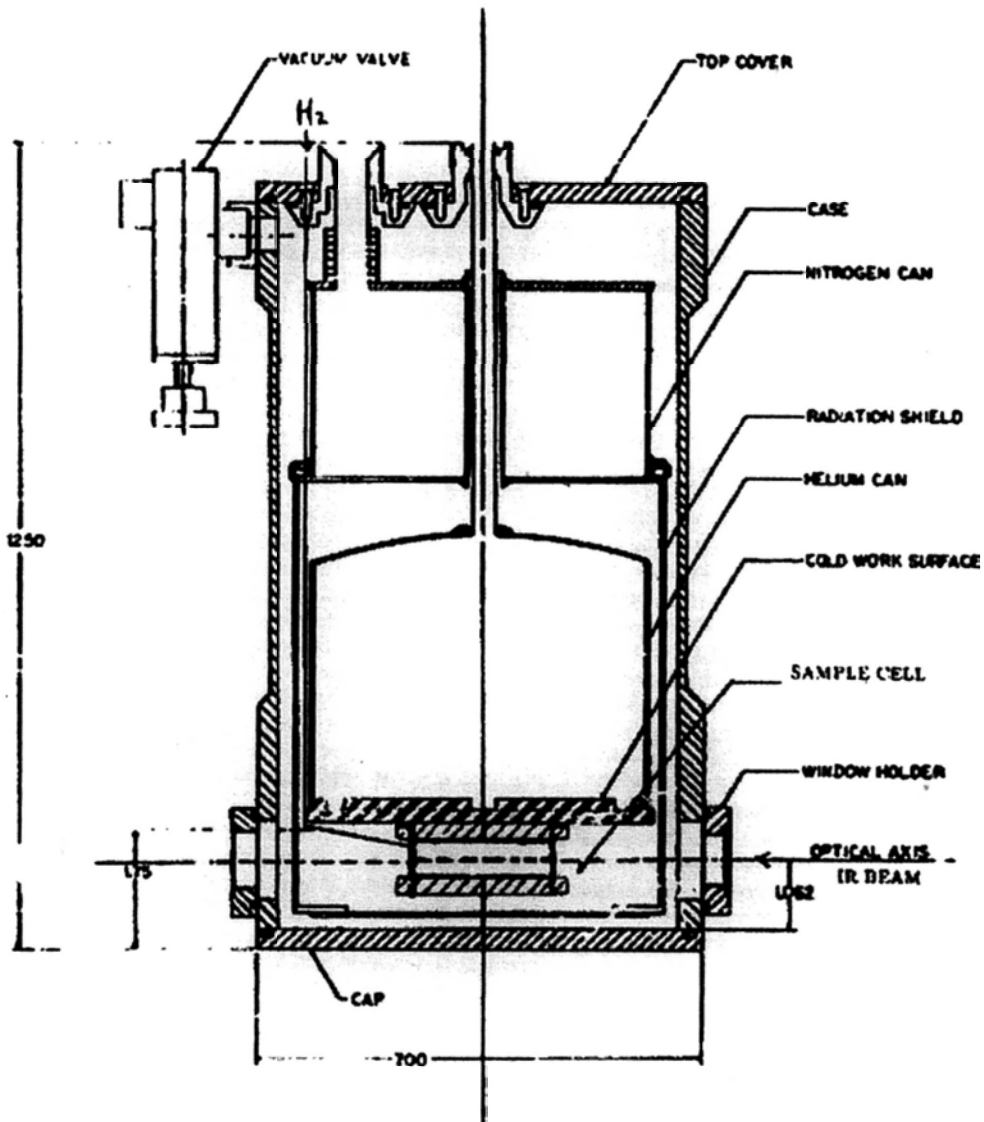


FIGURE 5. Liquid helium Dewar that accommodates the samples.

to monitor the temperature of the sample. Because of the good thermal conductivity of solid hydrogen, sapphire windows, and OFHC copper, their temperature difference is expected to be less than 0.5 K. The cell temperature was measured to be  $\sim 4.5$  K with liquid He bath under atmosphere due to the absorption of heat through the windows from the surroundings.

In studying the matrix-isolation spectroscopy in solid *para*-H<sub>2</sub>, an OFHC copper holder of 5 mm thickness with 20 mm clearance was installed on the cold surface of Dewar. Either BaF<sub>2</sub> or sapphire windows of 1 inch in diameter were glued to the holder using cryogenic conductive epoxy. Similarly, the sample temperature was measured by a diode temperature sensor (Lakeshore Cryotronics 670-SD) installed on the copper holder. The typical temperature of the cell was about 4.8-5.0 K.

### **III.1.4. Solid sample preparation**

The solid samples were deposited from gas onto the sample holders at a temperature range of 4.5 to 8 K. The solids obtained under this condition appeared to be visually transparent with reproducible optical and spectroscopic properties.

In filling the 3-cm cell with solid *para*-H<sub>2</sub>, the main difficulty is to minimize the temperature fluctuation of the cell during the growth process. Since the volume contraction of solid H<sub>2</sub> is about 20% when cooling from 14 to 4.2 K, cracks of the solid results in case that solid H<sub>2</sub> is prepared at melting point followed by cooling. An empirical approach to get around this difficulty is to fill the cell by applying successive gas pulses so that its temperature is maintained at around 7 K throughout the growth process. After the growth has been completed, the cell was cooled down to liquid He temperature. This approach is applicable because the volume change of solid H<sub>2</sub> from 7 to 4.2 K is much less. In practice, however, it has been found that the

sensor reading of 10.5 to 11 K produces *para*-H<sub>2</sub> crystal with the best optical quality without visual defects. At higher temperature, the solid cracked during cooling process.

The deposition of matrix samples was carried out by flowing mixture gas through a 200  $\mu\text{m}$  diameter nozzle at the end of the gas supply tube (1/16 inch O.D.), which was directed to outside of the Dewar by vacuum feedthrough and connected to vessel (B). In order to produce matrix film with uniform thickness with high transparency and reproducible optical quality, the deposition should not be too high. In practice, we found that placing the nozzle about 1.5 cm from the optical window with a gas flow rate of 12 sccm (controlled by a mass flow meter) gave the best results. Under these conditions, the deposition only raised the temperature of the holder by about 0.2 K.

## III.2. Spectrometers

Two infrared spectrometers have been used in the work presented here. A home-built high resolution near-infrared diode laser spectrometer was assembled from scratch to study the rovibrational  $W$  transition and a commercial Fourier-transform infrared spectrometer was used in studying the matrix spectroscopy in solid H<sub>2</sub>. The details of these two spectrometers will be discussed below.

### III.2.1. Diode laser spectrometer

The basic principle of diode laser can be found in a number of excellent reviews<sup>39</sup> and will not be repeated here. The block diagram of our home-built diode laser spectrometer is shown in FIGURE 6. The light source was a commercial tunable diode laser (Newport, 2010M) centered at 1500 nm with an external

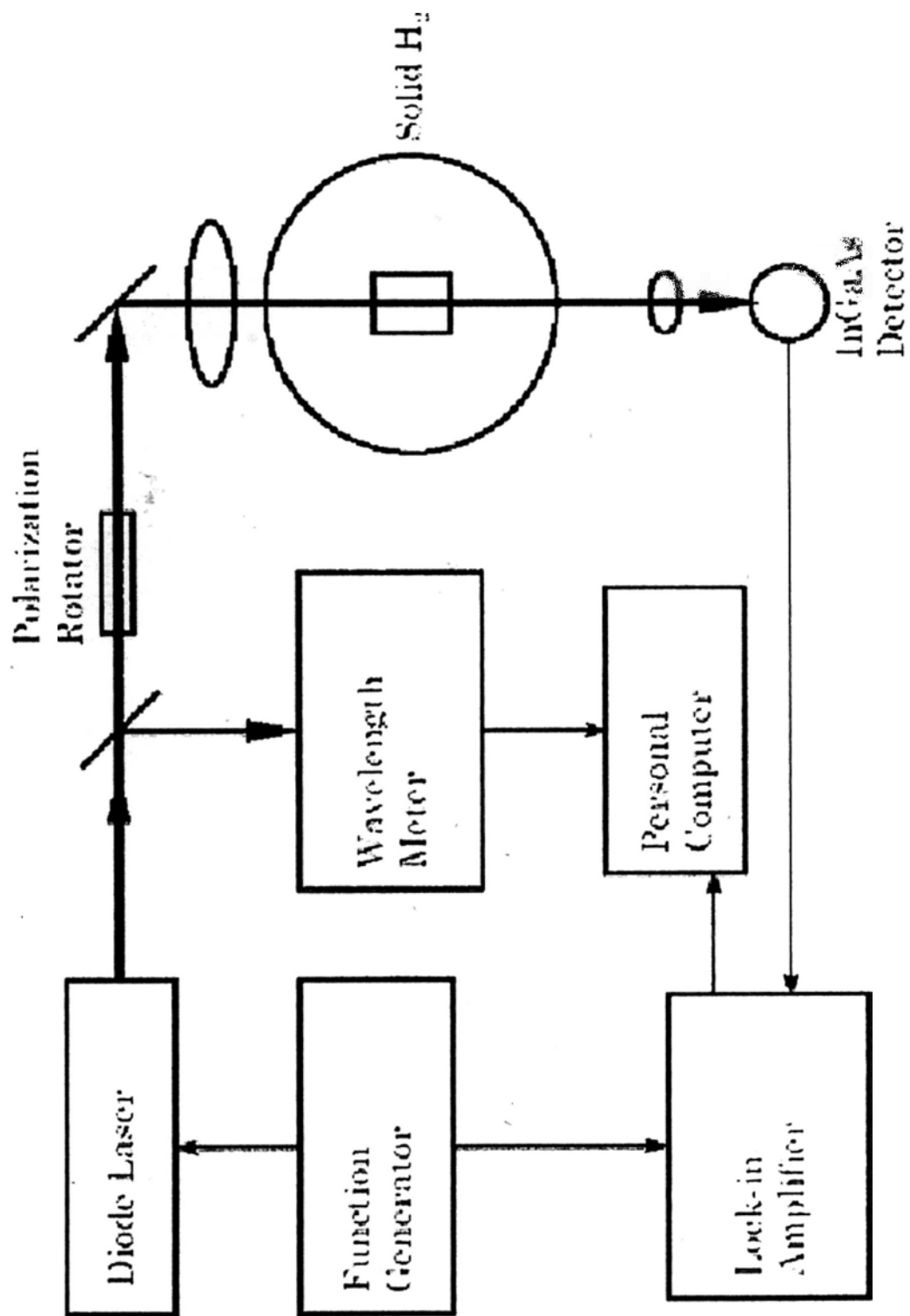


FIGURE 6. Schematic diagram of the experimental setup for near infrared diode laser spectrometer

Littman-Metcalf cavity, in which a diffraction grating is used to diffract the output beam of a laser diode into a tuning mirror driven by a piezoelectric transducer (PZT) to achieve a spectral purity of a few MHz. The laser beam is split into two parts: about 5% of the laser beam was used for laser frequency calibration while the main beam was used for spectroscopic studies.

The laser output frequency was calibrated using a wavelength meter (Burleigh, WA1500) at a resolution of  $0.001 \text{ cm}^{-1}$  and a spectrum analyzer (Thorlabs Inc.) with a free spectral range of 1500 MHz. In order to examine the practical frequency accuracy of the laser spectrometer,  $\text{CO}_2$  gas was used as a reference and its absorption frequencies were measured and compared with the values from Hitran database. As a result, it was found that repeating scans have an uncertainty of  $\sim 0.001 \text{ cm}^{-1}$ .

The main beam was loosely focused on the samples using a  $\text{CaF}_2$  lens. The exit beam was then tightly focused using a  $\text{CaF}_2$  lens on an InGaAs detector (Thorlabs Inc. Det410). The absorption signals were processed using phase sensitive detection by either amplitude modulation or frequency modulation of the laser output. In the former, a mechanical chopper at a frequency of 6 kHz was used to modulate the laser beam in front of the detector to achieve a sensitivity of  $\Delta I/I \sim 10^{-3}$ . In the latter, a sinusoidal voltage at 1 kHz from a generator (Stanford Research System, DS345) was sent to the laser controller to modulate the ramp voltage (for frequency tuning) of the piezoelectric driver. This modulation corresponds to fast switching the laser output frequency back and forth at a frequency of 1 kHz. The detected signals were then demodulated using a lock-in amplifier (Stanford Research System, SR830) referenced at the modulation frequency of 1 kHz. Using this demodulation scheme, the first derivative-type line shape can be observed using  $1f$  detection and second

derivative-type line shape was observed using  $2f$  detection. The effective resolution of frequency modulation was determined by the modulation depth, *i.e.* the peak-to-peak voltage of the sinusoidal function. The resolving power is improved by reducing the modulation depth. The typical sensitivity achieved by frequency modulation is about of  $\Delta I/I \sim 10^{-4}$  to  $10^{-5}$ . Compared to amplitude modulation, frequency modulation provides a better effective resolution as well as better sensitivity. It was found that at a modulation depth corresponding to a laser frequency shift of  $\pm 40$  MHz and below, clear splitting was observed in both  $1f$  and  $2f$  spectra of the W transition of solid  $H_2$ . Therefore, most spectra reported in our studies were recorded using a frequency modulation corresponding to  $\pm 40$  MHz unless specified. An in-house data acquisition program for frequency calibration and data averaging, processing, and storage was written using Labview programming language.

### **III.2.2. Fourier-transform infrared (FTIR) spectrometer**

Fourier-transform infrared (FTIR) spectroscopy is based on the Michelson interferometer, in which two coherent optical beams of equal intensity but different optical path generate interference pattern that is a unique function of optical path difference. A frequency spectrum can then be obtained by performing the Fourier transformation. FIGURE 7 shows the schematic diagram of a Michelson interferometer. Light beam emitted from the infrared source was split into two equal components by a beam splitter. A component is reflected to a mirror fixed in position while another component transmits through the beam splitter to reach the movable mirror whose separation from the beam splitter varies periodically. The two beams from the mirror then combine to produce interference pattern as a function of optical path difference. In case a broad band light source is used, different interference

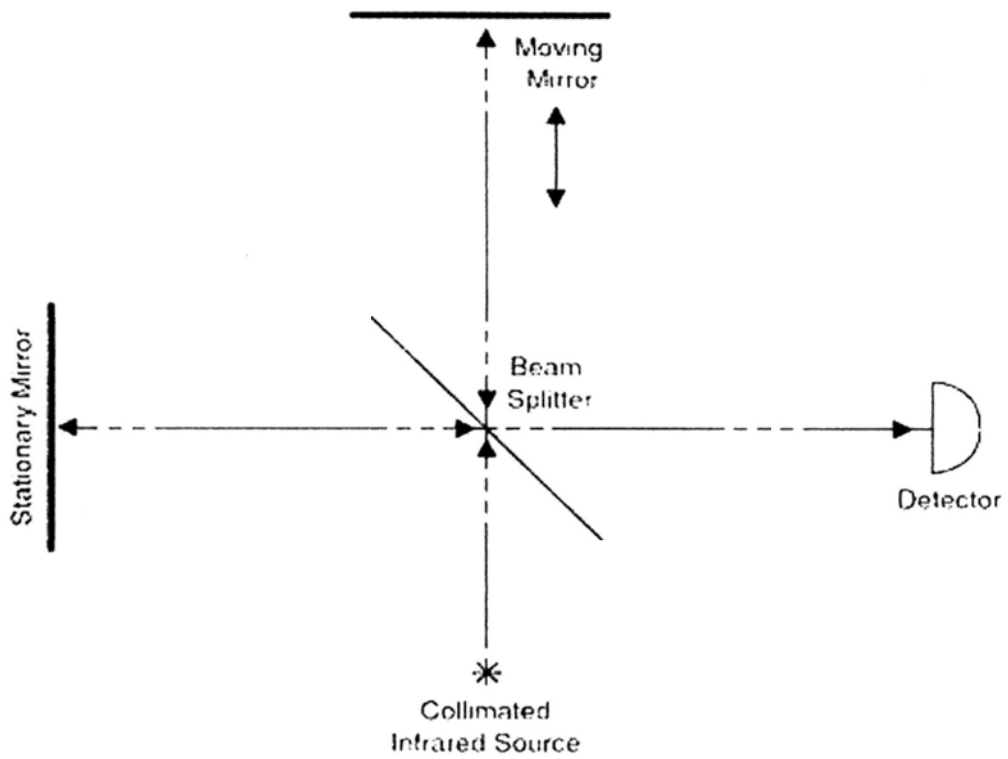


FIGURE 7 Schematic diagram of Michelson interferometer. Optical path difference is produced by moving of movable mirror.

pattern is obtained for different frequency. The overall signal detected will give a unique spectrum as a function of optical path difference, *i.e.* the interferogram. The frequency spectrum can be obtained by performing Fourier transformation of the interferogram.

Compared to a conventional grating spectrometer, Fourier-transform infrared spectrometer greatly improves the sensitivity and resolution. These improvements are achieved due to the following advantages of FTIR spectroscopy:

(a) The first advantage of FTIR is known as the Fellgett advantage based on the multiplex principle. In FTIR spectroscopy, all frequencies are measured simultaneously at all time by a single detector whereas in conventional instruments only a very narrow spectral region selected by the grating/prism is detected. As a result, the signal-to-noise ratio (S/N) for a given resolution and observation time using FTIR can be improved by a factor of  $\sqrt{N}$ , where  $N$  is the number of spectral elements selected by grating. In other words, FTIR achieves the spectrum of the same quality as grating spectrometers in much shorter time. In fact, an FTIR spectrum can be obtain in less than a second.

(b) The second advantage of FTIR is known as the Jacquinot advantage. FTIR spectrometer has a much higher optical throughput because of the absence of frequency selection. Thus, it results in much lower noise levels, and again, a higher S/N compared to conventional infrared spectrometers.

(3) The third advantage of FTIR is known as the signal averaging. The fast scans in FTIR spectrometer enable co-addition of many spectra in a short time. By repeating the measurements, random noise in the measurements is averaged out to give better S/N in FTIR spectroscopy.

(4) The forth advantage of FTIR is known as the Connes advantage. FTIR

spectrometer provides much better absolute frequency calibration. By employing a frequency-stabilized He-Ne laser as an internal wavelength calibration standard, the frequency uncertainty of  $0.001\text{ cm}^{-1}$  can be achieved.

The development of fast personal computers makes modern FTIR spectrometers more affordable since the complicated mathematical procedures involved in Fourier transformation can be completed in seconds using low cost powerful pc's. The detailed discussion of FTIR spectroscopy can be found in a number of excellent textbooks.<sup>53</sup>

The commercial FTIR spectrometer used in this work was a Bruker Vertex 70 FTIR spectrometer. By using different combinations of source, beam splitter, and detector, the frequency coverage of  $400$  to  $25000\text{ cm}^{-1}$  can be realized. The highest resolution of  $0.2\text{ cm}^{-1}$  can be obtained.

Due to the large size of our cryostat, the light source of FTIR spectrometer was directed out of the instrument and external detectors were used. A block diagram of the optical layout of our experiment is given in FIGURE 8. Since light beam was focused to a  $0.5\text{ mm}$  spot on the sample, different parts of the solid samples could be examined. A typical spectrum was recorded at  $0.2\text{ cm}^{-1}$  resolution with 1000 co-additions. In order to perform measurement in the different spectral region, two combinations of optical components in Vertex 70 FTIR spectrometer have been used. In recording spectra of solid  $\text{H}_2$  in the region of  $3000$ - $10000\text{ cm}^{-1}$ , a tungsten lamp, a  $\text{CaF}_2$  beam splitter and an external liquid  $\text{N}_2$  cooled InSb detector was used. On the other hand, a globar source, a KBr beam splitter and external liquid  $\text{N}_2$  cooled HgCdTe detector was used for recording the spectra of  $\text{NH}_3$  in solid  $\text{H}_2$  in the  $10\ \mu\text{m}$  region. In order to minimize the effect due to atmospheric absorption, the complete optical path was purged with dry  $\text{N}_2$  gas.

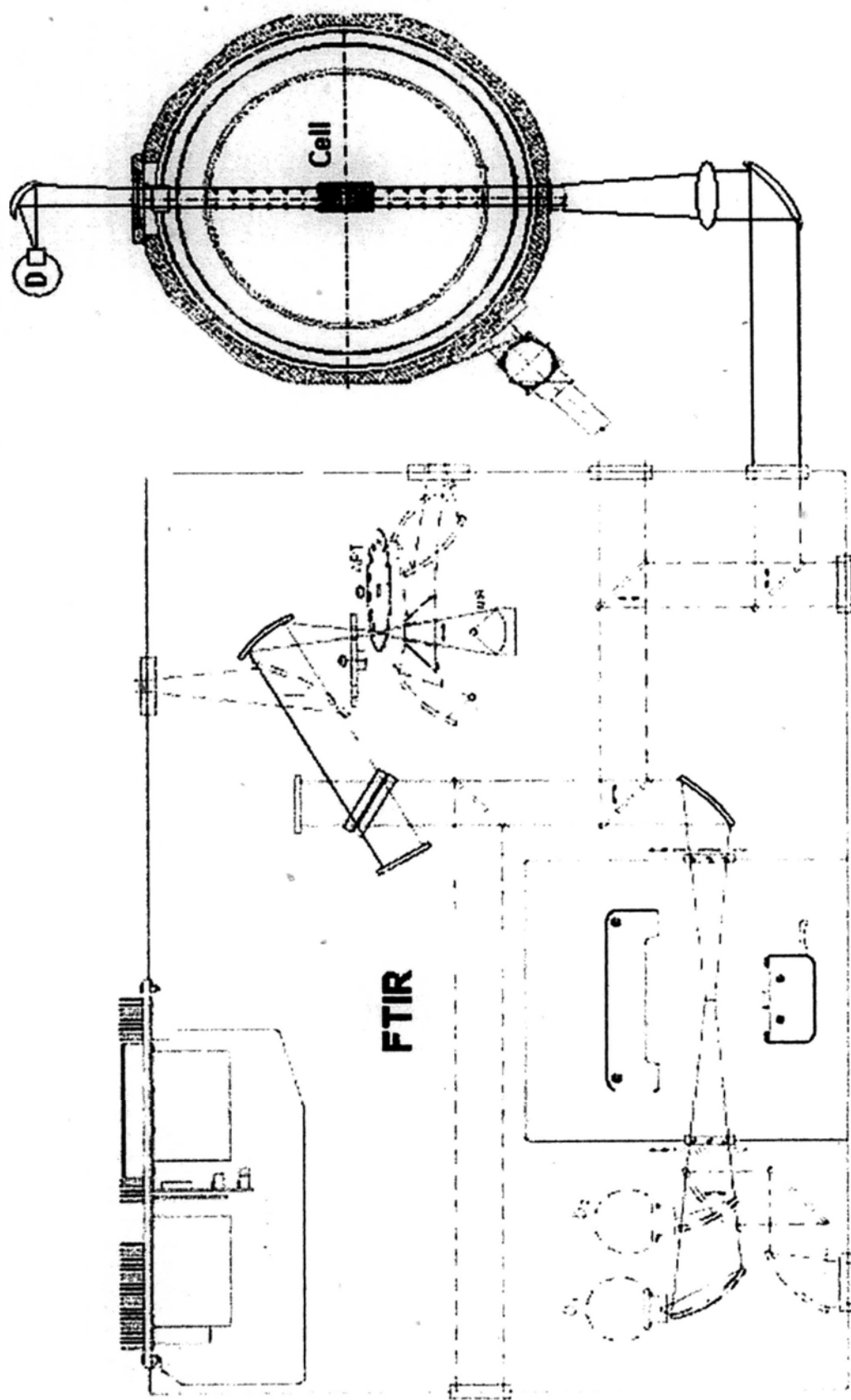


FIGURE 8 Schematic diagram of the experimental setup for Bruker Vertex 70 FTIR spectrometer

# CHAPTER IV. Tetrahexacontapole-induced Rovibrational $W$ Transition of Solid Parahydrogen

## IV.1. Background

The  $W$  ( $\Delta J = 6$ ) transition of solid hydrogen was attributed to the dipole moment induced by the tetrahexacontapole (64-pole) moment. The observation of both pure rotational  $W_0(0)$  transition and rovibrational  $W_1(0)$  transition of solid parahydrogen was first reported in 1989 using Fourier-transform infrared spectroscopy at moderate resolution of  $0.02 \text{ cm}^{-1}$ .<sup>14</sup> Due to the small vibrational dependence of 64-pole moment, the  $W_1(0)$  transition is weaker than the  $W_0(0)$  transition by a factor of  $\sim 3$ . Applying high resolution difference frequency laser spectroscopy, the pure rotational  $W_0(0)$  transition was resolved into a triplet whose relative intensity varied depending on the laser polarization.<sup>25</sup> This triplet structure was then interpreted as the splitting of  $M$  sublevels in the  $J = 6$  manifold by anisotropic crystal field interactions. The observed splitting was quantitatively accounted by assuming that the excitation energy is localized on the central molecule for extended time. This localization of the  $J = 6$  roton was realized by considering the fact that the dissipation of the excitation energy from the central  $\text{H}_2$  molecule to the surrounding molecules is very slow because (a) the resonance hopping between  $\text{H}_2$  molecules requires the very weak 64pole-64pole interaction with  $R^{-12}$  dependence that drops off quickly with increasing intermolecular separations and (b) the energy mismatch between the Debye frequency and the excitation energy leads to slow

roton-phonon energy transfer. While the localization of the exciton energy has been observed in the high resolution spectra of pure vibrational transitions of isotopic impurities such as *ortho*-H<sub>2</sub>, *ortho*-D<sub>2</sub>, *para*-D<sub>2</sub>, and HD in solid *para*-H<sub>2</sub> to give important information on intermolecular interactions with unprecedented accuracy,<sup>68</sup> the localization of the  $J = 6$  roton represents the first case in which excitation energy was localized on the host molecule in the solid state.

Based on the localization of the  $J = 6$  roton in the  $W_0(0)$  transition, it is expected that the rovibrational  $W_1(0)$  transition of solid *para*-H<sub>2</sub> also exhibit the same splitting pattern similar separation. Nevertheless, splitting of  $W_1(0)$  transition has never been observed in the previous studies. Applying near infrared diode laser spectroscopy, in the samples containing 2% of *ortho*-H<sub>2</sub>, the  $W_1(0)$  peak was observed at around 6441 cm<sup>-1</sup> with an overall width of 0.014 cm<sup>-1</sup> together with a bush of satellite lines by Oka and coworkers.<sup>69</sup> The electric quadrupole-quadrupole (EQQ) interaction between an excited *para*-H<sub>2</sub> molecule ( $\nu = 1, J = 6$ ) and a nearby  $J = 1$  *ortho*-H<sub>2</sub> molecule was considered as the main intermolecular effect for these satellite lines. In addition, using high-resolution FTIR spectroscopy, Steinhoff *et al.* observed the  $W_1(0)$  transition with a linewidth of 0.036 cm<sup>-1</sup> in 99.93% *para*-H<sub>2</sub> solid samples.<sup>16</sup> The plausible reasons for not observing the fine structure in the  $W_1(0)$  transition in the previous experiments may be ascribed to: (a) line broadening due to high *ortho*-H<sub>2</sub> content in the sample, (b) insufficient resolution of instruments, and/or (c) the breakdown of the localized exciton model in the rovibrational  $W$  transition due to mixing with double transitions as in the case of rovibrational  $S_\nu(0)$  transitions.<sup>70</sup>

The goal of our study is to clarify the model of localized exciton in the  $W_1(0)$  transition of solid *para*-H<sub>2</sub>. Taking advantage of high resolution afforded by near infrared diode laser spectroscopy together with the highly pure *para*-H<sub>2</sub> (~99.95%)

generated from our converter, the  $M$  splitting of the  $W_1(0)$  transition of solid *para*-H<sub>2</sub> has been observed. The corresponding crystal field parameters, determined using least-squares fitting, provide unambiguous evidence to support the localization of the  $J = 6$  rotons in both  $W_0(0)$  and  $W_1(0)$  transitions. Furthermore, the temperature dependence of the absorption frequencies has been studied in the range of 2.7 to 8.0 K. The details of these studies are presented in this chapter.

## IV.2. Theoretical Aspects

### IV.2.1. Crystal field splitting

In this section, the crystal field splitting of an excited molecule ( $v = 1, J = 6$ ) surrounded by ground state hydrogen molecules arranged in *hcp* symmetry (FIGURE 9) will be considered. Since there is no significant overlap in electron clouds between the excited molecule and the crystal, the main interaction to be considered is the long-range electrostatic interaction. Moreover, there is no permanent dipole and higher order multipoles for  $J = 0$  hydrogen molecules due to the spherically symmetric rotational wavefunction, interactions due to permanent multipole-multipole do not exist and thus have no contribution to the crystal field splitting. In other words, the first-order interaction in Equation (II-17) is zero. On other hand, a variety of intermolecular interactions by second-order perturbation, such as induction and dispersion, are responsible for producing the crystal field splitting. According to the expression of interaction potential mentioned in Chapter II, the general form of anisotropic interactions between H<sub>2</sub> molecules 1 and 2 regardless of the nature of interaction, can be expanded as

$$V(R, \omega_1, \omega_2) = \sum_{l_1, l_2, m} A_{l_1 l_2 m}(R) C_{l_1 m}(\omega_1) C_{l_2 \bar{m}}(\omega_2) \quad (\text{IV-1})$$

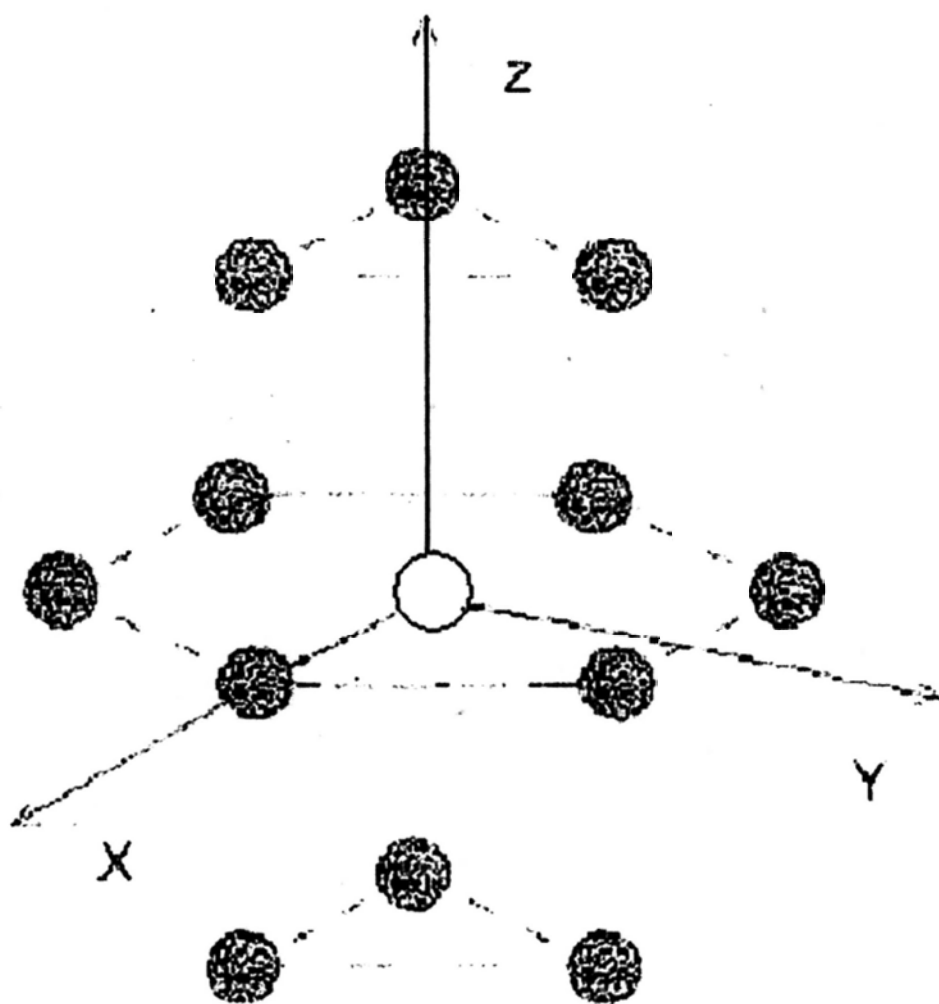


FIGURE 9 Crystal structure of an excited  $\text{H}_2$  molecule ( $\nu = 1, J = 6$ ) in the *hcp* crystal environment consisting of the ground state hydrogen molecules ( $\nu = 0, J = 0$ ). The filled circles indicate the  $\nu = 0, J = 0$  nearest neighbor  $\text{H}_2$  molecules and the small empty circles indicate a  $\nu = 1, J = 6$  excited  $\text{H}_2$  molecule.

where  $R$  is the separation between the molecules 1 and 2,  $\omega_1$  and  $\omega_2$  stand for the polar angles with respect to the pair axis, the coefficient  $A_{l_1 l_2 m}$  is the expansion coefficient which is a function of intermolecular separation  $R$  only, and  $C_{lm}$  are the spherical harmonics<sup>30</sup>. Due to the symmetry of hydrogen molecules, the values of  $l_1$  and  $l_2$  are limited to even integers. For both  $H_2$  molecules in the ground state of  $J_1 = J_2 = 0$ , the anisotropic effect of the extra binding energy is zero due to all the vanishing matrix elements in Equation (IV-1). Assuming molecule 1 in the  $\nu = 1, J = 6$  state while molecule 2 in the  $\nu = 0, J = 0$  state, the matrix elements in Equation (IV-1) is nonvanishing only when  $l_2 = m = 0$ . The anisotropic interactions is thus reduced as

$$V(R, \omega) = \sum_{l=0,2,4,\dots} A_{l00}(R) C_{l0}(\omega) \quad (\text{IV - 2})$$

Here we drop the index for the rovibrationally excited molecule 1. Terms with  $l = 0$  again corresponds to an angle independent interaction that is absorbed in the vibrational energy shift. By summing the effect of all the surrounding  $J = 0$  molecules, the total anisotropic crystal field interaction of molecule 1 is given as

$$V(R, \omega) = \sum_{i=2}^N \sum_{l=2,4,\dots} A_{l00}(R_i) C_{l0}(\omega_i) \quad (\text{IV - 3})$$

where  $R_i$  and  $\omega_i$  specify the distance and orientation of the vector connecting the  $i$ th molecule and the central  $J = 6$  molecule. With respect to the crystal frame and taking into account the  $D_{3h}$  symmetry for *hcp* crystals, we have

$$\begin{aligned} V(\Omega) &= \sum_{i=2}^N \sum_{l=2,4,\dots} A_{l00}(R_i) \sum_{m=-l}^l C_{lm}(\Omega) C_{lm}^*(\Omega_i) \\ &= \sum_{l=2,4,\dots} \sum_{i=2}^N B_l(R_i) C_{l0}^*(\Omega_i) C_{l0}(\Omega) \end{aligned}$$

$$= \sum_{l=2,4,\dots} \varepsilon_{lc} C_{l0}(\Omega) \quad (\text{IV - 4})$$

where the angle  $\Omega$  and  $\Omega_i$  are the orientation of the central molecule and the vector  $R_i$  in the crystal frame. Considering the two lowest order terms, an effective anisotropic crystal field interaction can be written as

$$V_c(\Omega) = \varepsilon_{2c} C_{20}(\Omega) + \varepsilon_{4c} C_{40}(\Omega) \quad (\text{IV - 5})$$

Including the angle-independent transition frequency  $\nu_0$ , the Hamiltonian of the transition frequency can then be expressed in the form

$$H = \nu_0 + \varepsilon_{2c} C_{20}(\Omega) + \varepsilon_{4c} C_{40}(\Omega) \quad (\text{IV - 6})$$

with three experimentally determined parameters. According to *ab initio* calculations by Mulder *et al.*<sup>72</sup> and the corresponding modification by van Kranendonk<sup>30</sup>,  $\varepsilon_{2c}$  assumes the form

$$\varepsilon_{2c}(R_i) = - \sum_{i=2}^N \left[ \frac{1.368}{R_i^6} e^2 a_0^5 + \frac{50.53}{R_i^8} e^2 a_0^7 + \frac{1185.0}{R_i^{10}} e^2 a_0^9 \right] C_{20}(\Omega_i) \quad (\text{IV - 7})$$

where dispersion interaction (the  $R^{-6}$  term) becomes the main contribution in the crystal field parameter  $\varepsilon_{2c}$ . In order to determine the value of  $\varepsilon_{2c}$ , the lattice sum is performed. By considering the first 20 shells of the molecules,  $\varepsilon_{2c}$  was determined to be  $-0.0022 \text{ cm}^{-1}$ . It was so small because the lattice sum from the first two layers accidentally vanishes in  $D_{3h}$  symmetry. Similarly, crystal field parameter  $\varepsilon_{4c}$  was determined to be  $-0.1124 \text{ cm}^{-1}$  using the expression

$$\varepsilon_{4c}(R_i) = - \sum_{i=2}^N \left[ \frac{2.44}{R_i^8} e^2 a_0^7 + \frac{46.3}{R_i^{10}} e^2 a_0^9 \right] C_{40}(\Omega_i) \quad (\text{IV - 8})$$

In contrast to the case of crystal field parameter  $\varepsilon_{2c}$ , both dispersion and induction contribute significantly to  $\varepsilon_{4c}$ , with the induction being the dominant

effect. In this calculation, the effect of molecular vibration is not considered. Based on the *ab initio* calculations of the quadrupole moments in the  $\nu = 0$  and  $\nu = 1$  states, an increase of about 10% in  $\epsilon_{4c}$  is expected upon vibrational excitation. The renormalization due to lattice vibration is not taken into account either. It has been known that this correction can be as great as 10 to 20%.<sup>30</sup>

#### IV.2.2. Selection Rules and Relative Intensities

The selection rules of the  $W$  transitions can be obtained using symmetry considerations. As discussed in Chapter II, the appropriate extended group  $G$  for an excited  $H_2$  molecule in otherwise  $J = 0$   $H_2$  molecules in an *hcp* crystal is composed only 24 *feasible* operations shown in Equation (II-5). As pointed out by Chan *et al.*, group  $G$  is isomorphic to  $D_{6h}$  with the character table shown in TABLE 2.<sup>25</sup> In this table, the symmetry classifications of the crystal-fixed components of the dipole moment  $\mu$  and the polarizability tensor  $\alpha$  are also given. The symmetry classification of the rotational levels of  $H_2$  molecules in group  $G$  were then obtained by considering their transformation under the operations of group  $G$  as discussed by Chan *et al.*<sup>25</sup> The results are summarized in TABLE 3. The thirteen  $M$  sublevels of the  $J = 6$  rotational states that are degenerate in isotropic space split into seven levels. Based on the results of TABLE 2 and TABLE 3, the symmetry of  $\mu_0(A_2'')$  and  $\mu_{\pm}(E')$  gives the selection rules  $\Delta M = \pm 3$  and  $\Delta M = \pm 2, \pm 4$ , respectively. In other words, only levels with  $|M| = 2, 3$ , and 4 in the  $J = 6$  manifold are allowed by the selection rules. When the light polarization is parallel to crystal  $c$  axis (*i.e.* the  $C_3$  rotational axis), only the  $|M| = 3$  transition is expected. On the other hand, perpendicular polarization gives rise to transitions corresponding to  $|M| = 2$  and 4 levels. A schematic of energy levels and the  $M$  splitting of  $W_1(0)$  transitions is illustrated in FIGURE 10, which for convenience is not drawn to scale.

TABLE 2 Character table of extended group  $G$

$\chi$	$E\bar{E}$	$2C_2\bar{E}$	$3C_2\bar{E}$	$E(\bar{12})$	$2C_1(\bar{12})$	$3C_1(\bar{12})$	$\sigma_h\bar{E}$	$2S_6\bar{E}$	$3\sigma_v\bar{E}$	$\sigma_h(\bar{12})$	$2S_6(\bar{12})$	$3\sigma_v(\bar{12})$	$(\bar{12})^*$
$SA_1'$	1	1	1	1	1	1	1	1	1	1	1	1	$a_{zz}, a_{xx} + a_{yy}$
$SA_2'$	1	1	-1	1	1	-1	1	1	-1	1	1	-1	-1
$SE'$	2	-1	0	2	-1	0	2	-1	0	2	-1	0	$(\mu, \mu, \mu)$
$SA_1''$	1	1	1	-1	-1	-1	1	1	1	-1	-1	-1	-1
$SA_2''$	1	1	-1	-1	-1	1	1	1	-1	-1	-1	1	1
$AE'$	2	-1	0	-2	1	0	2	-1	0	-2	1	0	0
$SA_1'''$	1	1	1	1	1	1	-1	-1	-1	-1	-1	-1	-1
$SA_2'''$	1	1	-1	1	1	-1	-1	-1	1	-1	-1	1	$\mu_{11}$
$SE''$	2	-1	0	2	-1	0	-2	1	0	-2	1	0	$(a_{xx}, a_{yy})$
$SA_1''''$	1	1	1	-1	-1	-1	-1	-1	-1	-1	-1	-1	-1
$SA_2''''$	1	1	-1	-1	-1	1	-1	-1	-1	-1	-1	1	1
$AE''$	2	-1	0	-2	1	0	-2	1	0	-2	1	0	0

TABLE 3 Classification of the rotational wavefunction in the group  $G$

Rotational quantum number	Symmetry
$J$ even	$s$
$J$ odd	$a$
$M = 0$ $J$ even	$sA'_1$
$J$ odd	$aA'_2$
$M \neq 0$ $ M  = 0 \pmod{6}$	$aA'_2$
$ M  = 1 \pmod{6}$	$E''$
$ M  = 2 \pmod{6}$	$E'$
$ M  = 3 \pmod{6}$	$aA'_2$
$ M  = 4 \pmod{6}$	$E'$
$ M  = 5 \pmod{6}$	$E''$

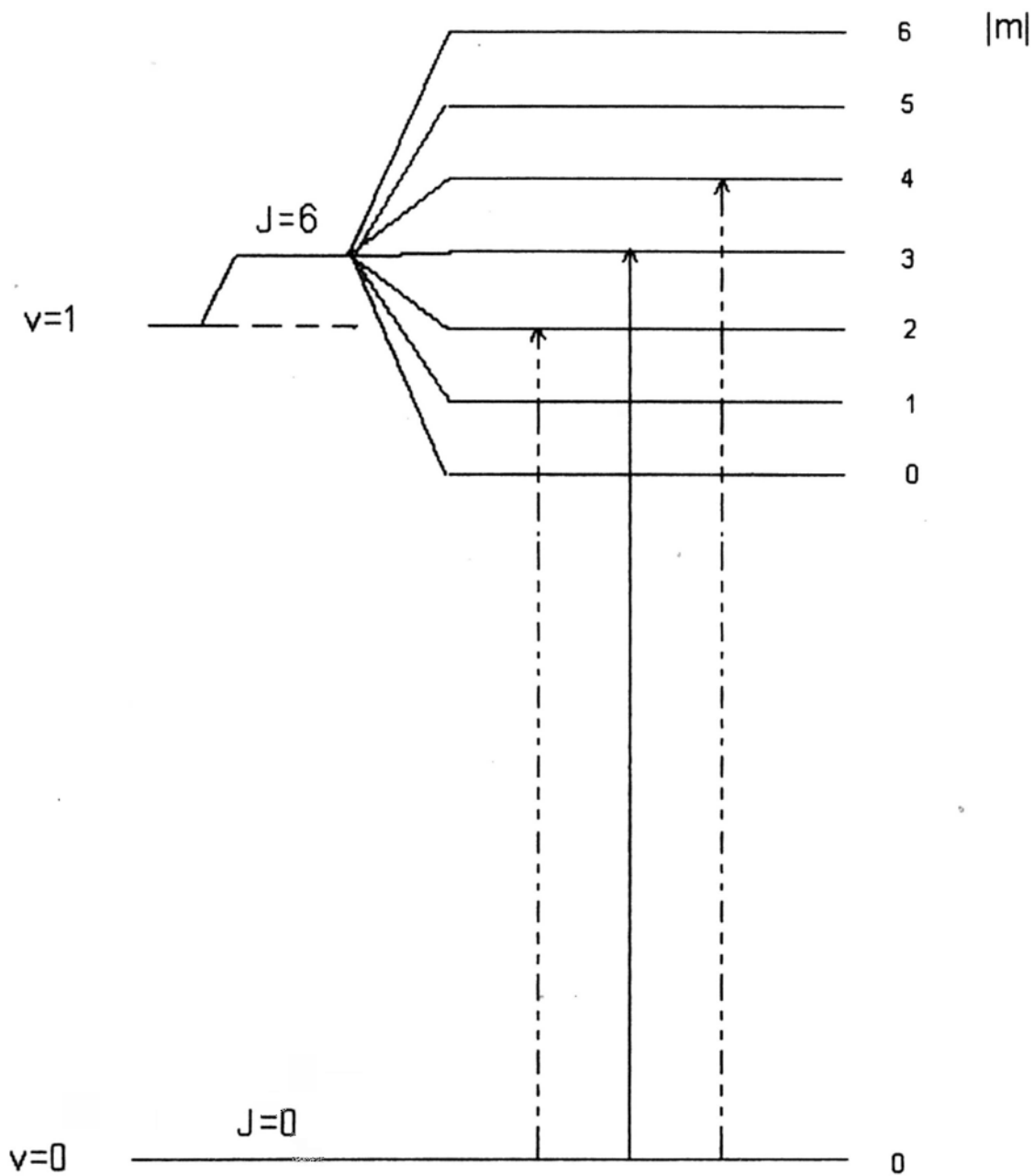


FIGURE 10 Schematic of energy levels with crystal field splitting for the  $W_1(0)$  transitions of solid hydrogen. The vertical solid arrows indicate the allowed transitions for light parallel to the  $c$  axis and the dotted perpendicular to the  $c$  axis.

Quantitative elucidation of the intensities of crystal field split components will help the assignment of transitions. Depending on the  $\nu$ th ( $\nu = 0, \pm 1$ ) component (64-pole)-induced dipole moment, the relative intensity of each  $M$  component can be calculated by the formula of Balasubramanian *et al.* expressed as<sup>73</sup>

$$\mu_\nu = 4\pi \sqrt{\frac{7}{15}} \frac{\alpha_{00} Q_{10}^{(6)}}{R_0^8} \sum_m C(617; m \nu m + \nu) Y_{6m}^* S_{7m+\nu} \quad (\text{IV - 9})$$

where  $S_{7m+\nu} = \sum_\rho \left[ \frac{R_0}{R_\rho} \right]^8 Y_{7m+\nu}^*(\Omega_\rho)$  is the dimensionless lattice sum with respect to the crystal frame,  $\alpha_{00} \equiv \langle \nu = 0, J = 0 | \alpha | \nu = 0, J = 0 \rangle$  is the isotropic polarizability of the  $J = 0$  molecules in the ground state,  $Q_{10}^{(6)} \equiv \langle \nu = 1, J = 6 | Q^{(6)} | \nu = 0, J = 0 \rangle$  is the transition 64-pole moment, all the angular dependence is referred to the crystal frame. Once again, the  $\mu_\nu$  operator in Equation (IV-9) represents dipole moment induced in the surrounding molecule through its isotropic polarizability by the 64-pole moment of the central molecule. The intensities can be calculated from  $\langle \langle J', M' | \mu_\nu | J, M \rangle \rangle^2$  using Equation (IV-9).

The invariance of the lattice sum based on the limitation of group symmetry requires that  $m + \nu = \pm 3$ . As a result,  $\mu_0$  gives rise to the transition with  $|M| = 3$ , so that the intensity should be expressed by squares of matrix elements  $\langle \langle 6, 3 | \mu_0 | 0, 0 \rangle \rangle$  and  $\langle \langle 6, -3 | \mu_0 | 0, 0 \rangle \rangle$ . On the other hand,  $\mu_{\pm 1}$  give rise to transitions with  $|M| = 2$  or 4, thus we determine the intensity of  $|M| = 2$  transitions by squares of matrix elements  $\langle \langle 6, -2 | \mu_{+1} | 0, 0 \rangle \rangle$  and  $\langle \langle 6, 2 | \mu_{-1} | 0, 0 \rangle \rangle$  whereas the intensity of  $|M| = 4$  transitions by squares of matrix elements  $\langle \langle 6, -4 | \mu_{-1} | 0, 0 \rangle \rangle$  and  $\langle \langle 6, 4 | \mu_{+1} | 0, 0 \rangle \rangle$ . Evaluating the lattice sum in Equation (IV-9), the ratio of the relative intensity of the three  $M$

components is given as:

$$I(|M| = 2) : I(|M| = 3) : I(|M| = 4) = 45 : 40 : 6 \quad (\text{IV} - 10)$$

for depolarized light. Our assignment of the observed spectrum was based on this polarization dependence.

### IV.2.3. Thermal effects

One of the most interesting observations in the spectroscopic study of solid hydrogen has been the extremely narrow spectral linewidths. This observation has led to the question "Is the observed linewidth homogeneous? If not, what is the homogeneous linewidth?". The temperature effect of the absorptions provides a wealth of information to shed light on our understanding of this issue. Since the observed transition frequency is shifted from the temperature independent gaseous value by a so-called matrix shift, *i.e.* the energy correction due to intermolecular interactions, the change of temperature will change the matrix shift as a result of changing the intermolecular separation. In other words, the absorption frequency is expected to have temperature dependence in solid H<sub>2</sub>. In addition, the changes in temperature also change the phonon-exciton interaction that will affect the relaxation rate and hence the linewidth and line shape.

In the case of solid hydrogen, the molar volume change at different temperature has been ascribed to the change of the observed temperature effects of absorption features. As measured by Krupskii<sup>74</sup> and his colleagues and also reported in the book of Souers<sup>26</sup>, the observed molar volume expansion/shrinkage of solid hydrogen yielded an empirical simple power law with the typical temperature dependencies:

$$\delta V(T) = V(T) - V(0) = 2.233 \times 10^{-6} T^{4.424} \text{ cm}^3 / \text{mol} \quad (\text{IV} - 11)$$

Where  $\delta V(T)$  is the temperature variation of molar volume of solid H<sub>2</sub>. Similarly,

this power law can be used for the thermal variation of frequency shifts, which should be expressed as:

$$\delta\nu(T) = \nu(T) - \nu(0) = \left( \frac{\partial\nu}{\partial V} \right) \delta V(T) = \text{const} \times T^{4.424} \quad (\text{IV} - 12)$$

where the factor  $\frac{\partial\nu}{\partial V}$  should be a constant, which depends on the intermolecular potential (as a function of intermolecular distance  $R$ ) that gives rise to the deviation of the energy levels of solid hydrogen from those of the isolated molecule. It is seen that the frequency shifts upon variation of the temperature are due to thermal contraction of the crystal and thus intermolecular forces. The above equation was first confirmed in the study of electric field induced  $Q_1(0)$  transition of solid hydrogen, in which a power of 4.096 was observed.<sup>75</sup> The observed frequency shifted up by 4.2 GHz from 4.9 to 13.5 K together with an increase of linewidth by a factor of  $\sim 3$ . In addition, a clear Lorentzian linewidth was observed at  $\sim 13$  K suggesting the homogeneous broadening was dominant while the Gaussian line shape observed at 4.2 K may be inhomogeneously broadened. The power law in frequency shift (Equation (IV-12)) was also observed for a number of transitions using high resolution FTIR spectroscopy.<sup>76</sup> On the other hand, the temperature effect of the Raman  $Q_1(0)$  transition of solid  $H_2$  measured under the condition of constant molecular density reported by Kuroda *et al.* has revealed that vibron-phonon interaction that is responsible for the relaxation process give rise to the  $T^4$  and  $T^7$  dependence of the frequency shift and linewidth, respectively.<sup>77</sup> Furthermore, the observed Lorentzian line shape in the range of 5.7 to 12 K strongly suggested the homogeneous broadening mechanism. In the case of  $W_1(0)$  transition, it will be interesting to see if the additional roton-phonon interaction may give rise to a faster relaxation process and how this process changes the temperature effect of the

transitions.

## IV.3. Results

### IV.3.1. Absorption spectrum

The  $W_1(0)$  transition of 3-cm long samples of 99.95% *para*-H<sub>2</sub> was observed at 6441.73 cm<sup>-1</sup> with an instrument-limited width of 0.16 cm<sup>-1</sup> in the FTIR spectrum as shown in FIGURE 11. From the spectrum, the integrated absorption coefficient  $\tilde{\alpha}$  defined by Equation (III-2) was measured to be  $1.02(10) \times 10^{-19}$  cm<sup>3</sup>/s, in good agreement with that reported by Okumura *et al.*<sup>14</sup>. Applying high resolution near infrared diode laser spectroscopy with amplitude modulation, the spectrum using parallel laser polarization exhibited asymmetric absorption line as shown in FIGURE 12(A). The absorption maximum was observed at 6441.7333 cm<sup>-1</sup> with a fractional absorption ( $\Delta I/I$ ) of ~5% and a width of 0.014 cm<sup>-1</sup> (FWHM). This spectral width was comparable to that of the  $W_0(0)$  transition under the same modulation scheme. By using perpendicular laser polarization, the absorption maximum was greatly reduced with a partially resolved peak at 6441.7189 cm<sup>-1</sup> as shown in FIGURE 12(B). Since the anisotropy of crystal environment imposes different selection rules for light with different polarization, the change of relative intensity with different laser polarization indicated that the partially resolved lines may be the  $M$  components split by the crystal-field interactions.

In order to fully resolve the features, frequency modulation was applied to improve the effective resolution. Traces (C) and (D) in FIGURE 12 show the spectra using  $2f$  demodulation scheme. The modulation depth corresponded to a laser frequency shift of about  $\pm 20$  MHz. In trace (C), the  $W_1(0)$  transition was resolved

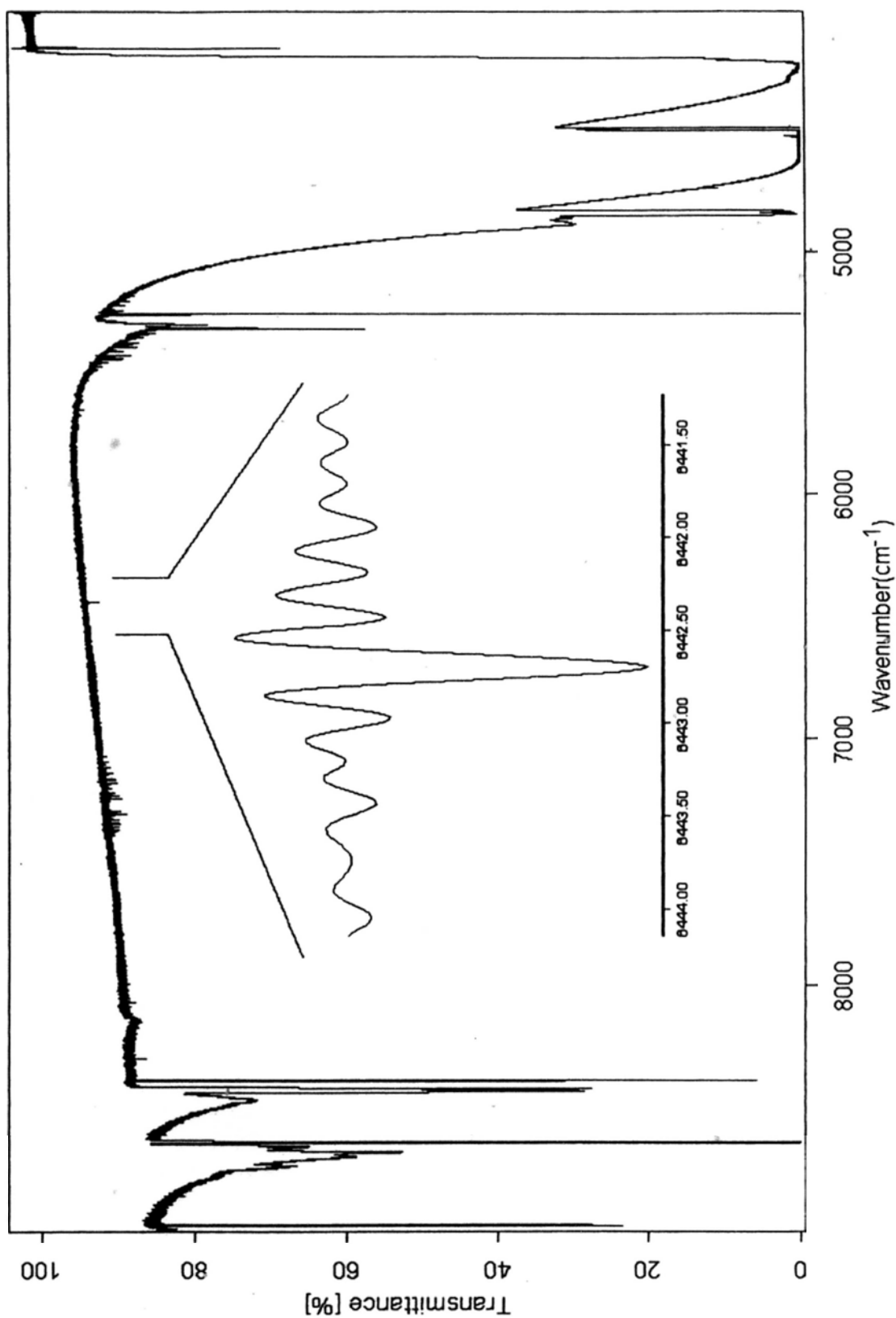


FIGURE 11 Overview of FTIR spectrum of ~99.95% solid *para*-H<sub>2</sub> samples at 0.2 cm<sup>-1</sup> resolution. The optical path is 3 cm. The line at 6442.75 cm<sup>-1</sup> in the enlarged region was assigned to the  $W_1(0)$  transition.

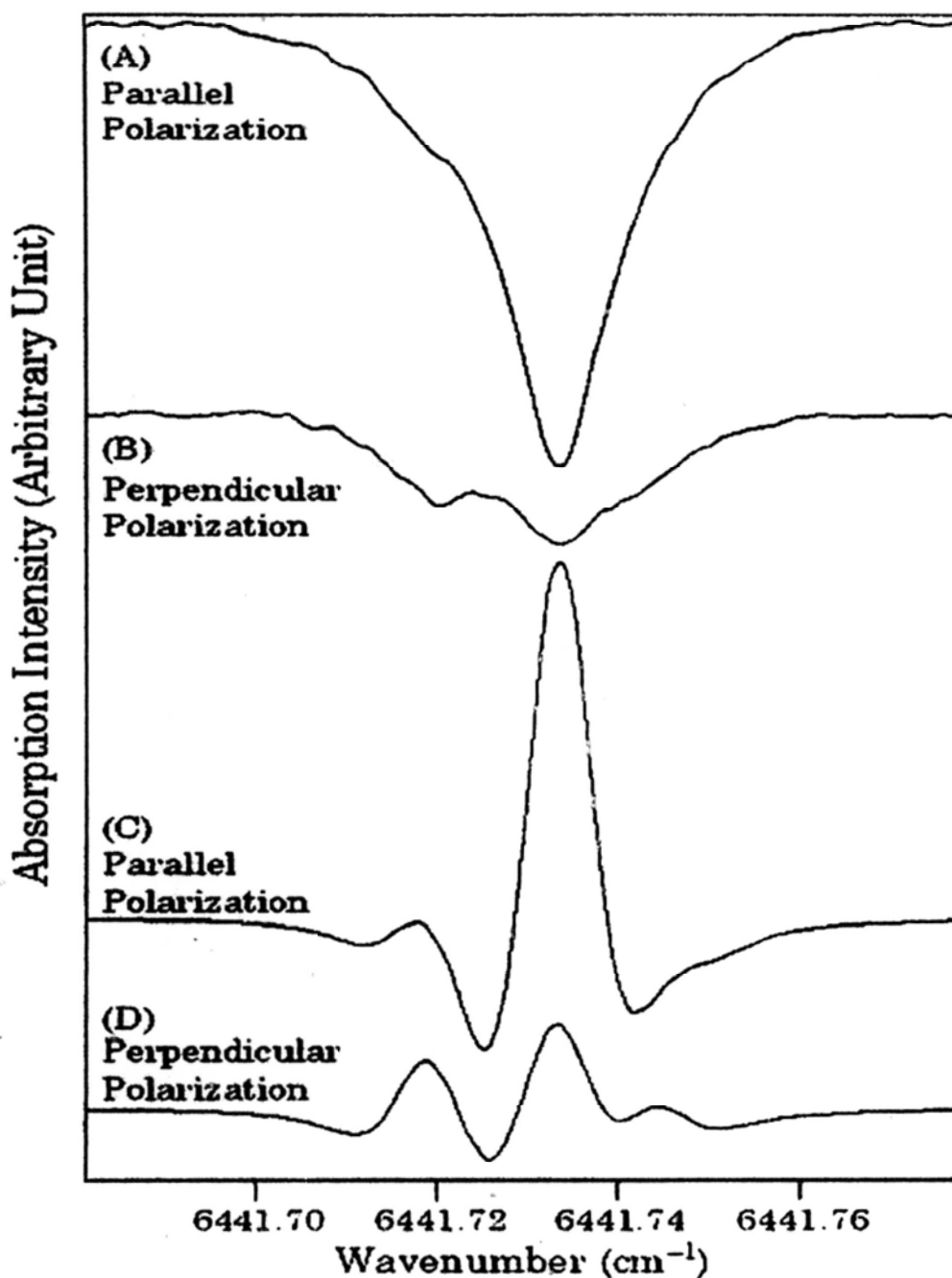


FIGURE 12 Laser polarization dependence of the  $W_1(0)$  transition of solid *para*-H<sub>2</sub>. The amplitude modulated spectra are shown in traces (A) and (B). To demonstrate the effect of laser polarization on intensity, both spectra are plotted using the same vertical scale. The  $2f$  frequency modulated spectra (C) and (D) are plotted in the same fashion. The small peak at 6441.7438 cm<sup>-1</sup> is only observed in  $2f$  spectra with improved resolution.

into only two main peaks at 6441.7189 and 6441.7333  $\text{cm}^{-1}$  using parallel laser polarization with an additional peak at 6441.7438  $\text{cm}^{-1}$  barely noticeable. On the other hand, the triplet structure was clearly shown using perpendicular laser polarization as shown in trace (D). The three peaks were observed at 6441.7189, 6441.7333, and 6441.7438  $\text{cm}^{-1}$ , respectively. A typical linewidth of about 100 MHz (FWHM) was observed in the  $2f$  modulation scheme. It should be noted that the profile shown in traces (C) and (D) do not represent the true line shape of  $W_1(0)$  transition but resemble the 2<sup>nd</sup> derivatives of the spectral transition observed in amplitude modulation because of the  $2f$  demodulation scheme.

The overall pattern of the  $W_1(0)$  transition was very similar to the  $W_0(0)$  transition with the observed splitting also around 0.01  $\text{cm}^{-1}$ . The three transitions were assigned to the  $|M| = 2, 3,$  and 4 levels in the  $J = 6$  manifold according the polarization dependence and relative intensity as discussed in Section IV.2.2. Since the transition at 6441.73  $\text{cm}^{-1}$  was the strongest component at parallel polarization and its intensity decreased significantly at perpendicular polarization, it was assigned to the  $|M| = 3$  transition. On the other hand, the components at about 6441.72 and 6441.74  $\text{cm}^{-1}$  gained intensities at perpendicular polarization as predicted for  $|M| = 2$  and 4 transitions. Based on the predicted relative intensity, they are assigned to  $|M| = 2$  at 6441.72  $\text{cm}^{-1}$  and  $|M| = 4$  at 6441.74  $\text{cm}^{-1}$ . These assignments are consistent with the analysis of  $W_0(0)$  transition as well as the crystal field parameters which are negative due to attractive van der Waals interactions.

A total of four samples of solid *para*-H<sub>2</sub> have been examined. The *ortho*-H<sub>2</sub> contents in these samples were  $\sim 0.05\%$ . The observed frequencies of the  $W_1(0)$  transition are listed in TABLE 4. As seen in the table, a variation on the order of 0.001  $\text{cm}^{-1}$  in absorption frequency was observed. This variation may be due to (a)

TABLE 4 Observed frequencies of the  $W_1(0)$  transition for different samples. The results of least-squares fitting are also listed with the corresponding uncertainty in parenthesis

Sample	Assignment	Transition frequency ( $\text{cm}^{-1}$ )	
		Observed	Cal. - Obs.
I	M = 2	6441.7189	-0.0005
	M = 3	6441.7333	-0.0002
	M = 4	6441.7438	+0.0008
II	M = 2	6441.7178	+0.0006
	M = 3	6441.7327	+0.0004
	M = 4	6441.7441	+0.0005
III	M = 2	6441.7185	+0.0001
	M = 3	6441.7333	+0.0002
	M = 4	6441.7449	-0.0003
IV	M = 2	6441.7183	+0.0001
	M = 3	6441.7332	-0.0001
	M = 4	6441.7456	-0.0010

Fitted Parameters ( $\text{cm}^{-1}$ )

$\nu_0$	6441.7256(14)
$\epsilon_{2c}$	-0.0286(83)
$\epsilon_{4c}$	-0.1048(95)
Variance	0.0006

the instrumental uncertainty of frequency measurement and/or (b) slightly different crystal defects in the samples as a result of small variation in the crystal growth conditions and *ortho*-H<sub>2</sub> contents. Based on the assignments discussed above, the three parameters  $\nu_0$ ,  $\varepsilon_{2c}$ , and  $\varepsilon_{4c}$  in Equation (IV-6) were determined by least-squares fitting using all observed frequencies in the four samples. As shown in TABLE 4,  $\nu_0$ ,  $\varepsilon_{2c}$ , and  $\varepsilon_{4c}$  were determined to be 6441.7256(14), -0.0286(83), and -0.1048(95) cm<sup>-1</sup>, respectively, with the corresponding uncertainty in parenthesis. The fitted value of  $\varepsilon_{2c}$  is about an order of magnitude greater than the theoretical value. This is not unexpected as its experimental values have been varied from -0.0562 to 0.0250 cm<sup>-1</sup> for different transitions.<sup>68</sup> Since  $\varepsilon_{2c}$  was determined theoretically based on the fact that the lattice sum from the first two layers accidentally vanishes in *D*<sub>3h</sub> symmetry, it is very sensitive to the symmetry of the crystals. Therefore, the great deviation simply indicates that crystals were not prepared with perfect *D*<sub>3h</sub> symmetry. The value of  $\varepsilon_{4c}$ , which was not severely affected by the imperfection of crystals, is in good agreement with the theoretical value based on Equation (IV-8). It appears to be slightly smaller than that reported for the *W*<sub>0</sub>(0) transition.<sup>25</sup> However, it should be noted that  $\varepsilon_{4c}$  reported in Ref. 25 was fitted by fixing  $\varepsilon_{2c} = -0.0058$  cm<sup>-1</sup>, a presumably underestimated value based on experimental observations<sup>68</sup>. For a better comparison, the *W*<sub>0</sub>(0) transition was refitted by setting  $\varepsilon_{2c} = -0.0286$  cm<sup>-1</sup>. The values of  $\nu_0$  and  $\varepsilon_{4c}$  were determined to be 2410.5282 cm<sup>-1</sup> and -0.09725 cm<sup>-1</sup>, respectively, in the new fit. It is seen that a factor of ~1.1 is obtained by comparing the values of  $\varepsilon_{4c}$  for the *W*<sub>1</sub>(0) and the *W*<sub>0</sub>(0) transitions. This ratio is consistent with the fact that there is an increase of about 10% in  $\varepsilon_{4c}$  arising from the quadrupole moment of the *J* = 6 molecule in  $\nu =$

1 state compared with that in  $\nu = 0$  states.<sup>25</sup> This agreement further confirmed the localization of  $J = 6$  rotons in both  $W_0(0)$  and  $W_1(0)$  transitions.

Intricate satellite structure near the  $W_1(0)$  transition previously observed in solid samples with  $\sim 2\%$  *ortho*-H<sub>2</sub> was not found in our samples. Since the *ortho*-H<sub>2</sub> concentration in our samples was about  $\sim 0.05\%$ , the chance of having a closely located pair of  $J = 6$  *para*-H<sub>2</sub> and  $J = 1$  *ortho*-H<sub>2</sub> molecules is expected to be very low.

### IV.3.2. Temperature effect

The temperature effect on the crystal field splitting of the  $W_1(0)$  transition was also studied in order to obtain information to further understand the interaction. FIGURE 13 shows the observed frequencies and linewidths of solid sample (I) at different temperature in the range of 2.7-8.0 K. The whole absorption pattern exhibited a positive shift of  $\sim 330$  MHz by raising the temperature from 2.7 to 8.0 K. This shift was reproducible for different samples and not affected by repeating the temperature cycle. The observed line positions of  $|M| = 3$  transition the transition were plotted versus temperature and displayed in FIGURE 14. Assuming the temperature dependence of line position following a power law:

$$\nu(T) = \nu(0) + a \times T^b \quad (\text{IV} - 13)$$

based on the temperature effect on the intermolecular separation  $R$  as discussed above, the parameters  $a$ ,  $b$ , and  $\nu(0)$  obtained by least-squares fitting were  $1.20(5)$  cm<sup>-1</sup>,  $4.39(20)$ ,  $6441.7326(1)$  cm<sup>-1</sup>, respectively. The power dependence  $b$  of temperature is in excellent agreement with the predicted value of 4.424 as discussed above. This agreement indicates that the temperature dependence of the absorption frequency of the  $W_1(0)$  transition is mainly due to the change of molar volume that in turn changes intermolecular interaction with  $R$  dependence.

In order to further investigate the temperature effects of isotropic and anisotropic intermolecular interactions on the frequency shift, the relative changes of absorption frequency for the  $M$  components of the  $W_1(0)$  transition at different temperature were also examined. As shown in TABLE 5, the observed crystal field splitting at different temperatures remained essentially constant within instrumental uncertainty. In other words, as the temperature was raised from 2.7 to 8.0 K, the excitation energy remained to be localized on the excited  $H_2$  molecule and all the three angle-dependent  $M$  components of the  $W_1(0)$  transition exhibited similar shift. This observation strongly suggests that the change of isotropic interactions is responsible for the temperature shift. To further verify this point, the angle-independent transition frequencies  $\nu_0$  at different temperatures determined by least-squares fitting using observed frequencies in the four samples were plotted against the temperature as shown in FIGURE 15. In analogy to Equation (IV-13), a power law for the temperature dependence of  $\nu_0$  in the form of:

$$\nu_0(T) = \nu_0(0) + a_0 \times T^{b_0} \quad (\text{IV - 14})$$

was obtained with the parameters  $a_0$ ,  $b_0$ , and  $\nu_0(0)$  fitted to  $9.23(3) \text{ cm}^{-1}$ ,  $4.49(20)$ ,  $6441.7245(7) \text{ cm}^{-1}$ , respectively. It is noted that the power dependence of temperature for  $\nu_0$  was close to the empirical value of 4.424 for molar volume. It is therefore little doubt that isotropic interactions are the main contribution for the frequency shift of the  $W_1(0)$  transition. The temperature of anisotropic interactions on frequency shift is much smaller that may not be observed with our instrumental uncertainty.

The temperature variation of the linewidth was not clearly observed. As shown in FIGURE 13, the linewidth fluctuated around  $0.0070 \text{ cm}^{-1}$ . This observed width may be dominated by inhomogeneous broadening due to crystal strain produced

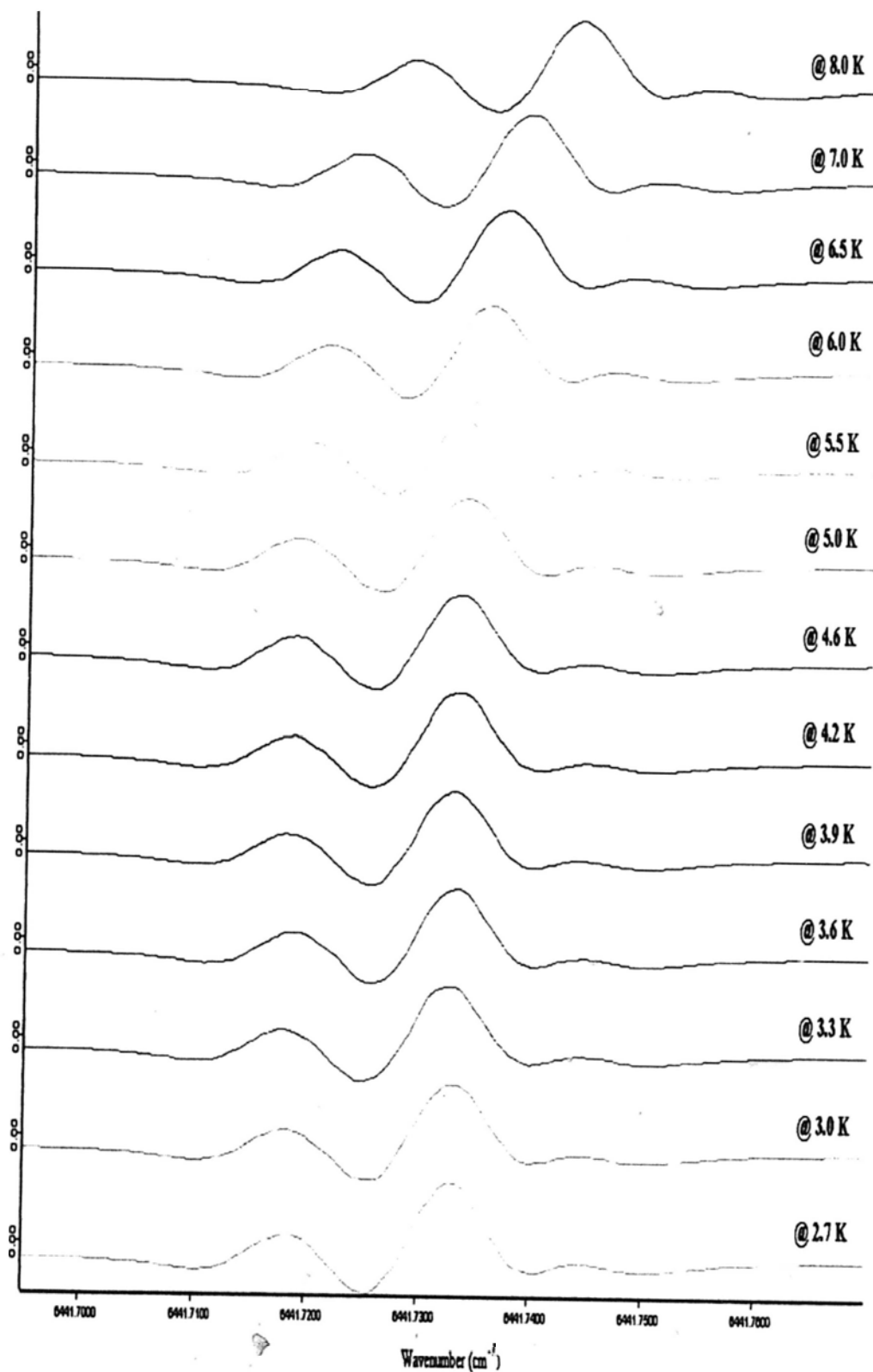


FIGURE 13 Observed temperature dependence of the  $W_1(0)$  transition of solid *para*-H<sub>2</sub>. The figure shows the spectral lines in the temperature range from 2.7 to 8.0 K.

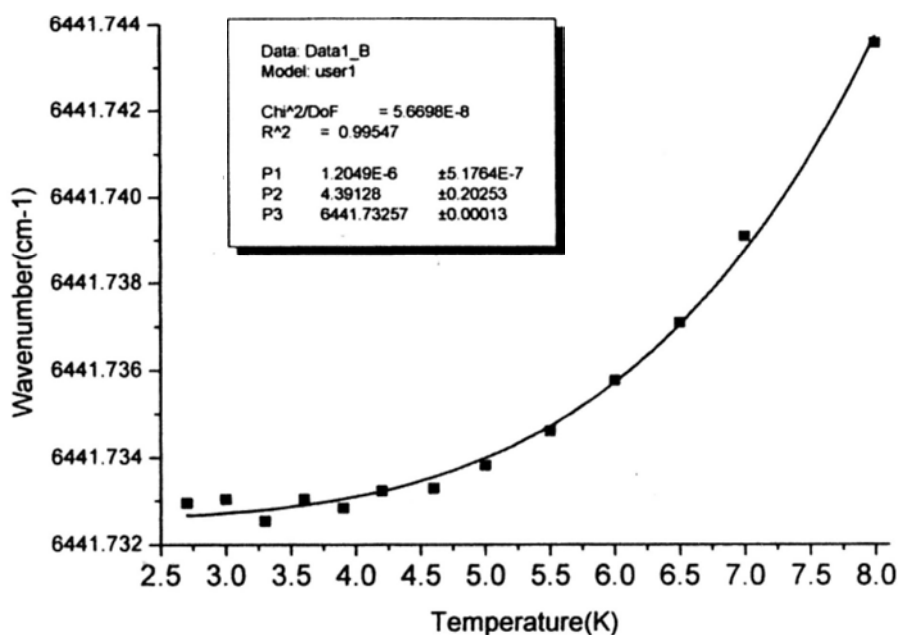


FIGURE 14 Frequency shift of the  $W_1(0)$  transition of solid *para*-H<sub>2</sub> as a function of temperature. The solid line shows the curve  $\nu(T) = 6441.7326 + 1.20 \times 10^{-6} \times T^{4.391 \pm 0.203} \text{ cm}^{-1}$ , which was obtained by least squares fitting method.

TABLE 5 Observed relative changes of frequencies for the  $M$  components of the  $W_1(0)$  transition in solid sample (I) at different temperatures.

Temperature (K)	$\nu( M =4)-\nu( M =3)$ ( $\text{cm}^{-1}$ )	$\nu( M =3)-\nu( M =2)$ ( $\text{cm}^{-1}$ )
2.7	0.0116	0.0148
3.0	0.0115	0.0151
3.3	0.0122	0.0150
3.6	0.0115	0.0147
3.9	0.0117	0.0149
4.2	0.0119	0.0153
4.6	0.0114	0.0149
5.0	0.0116	0.0154
5.5	0.0119	0.0149
6.0	0.0113	0.0147
6.5	0.0118	0.0153
7.0	0.0117	0.0152
8.0	0.0119	0.0149

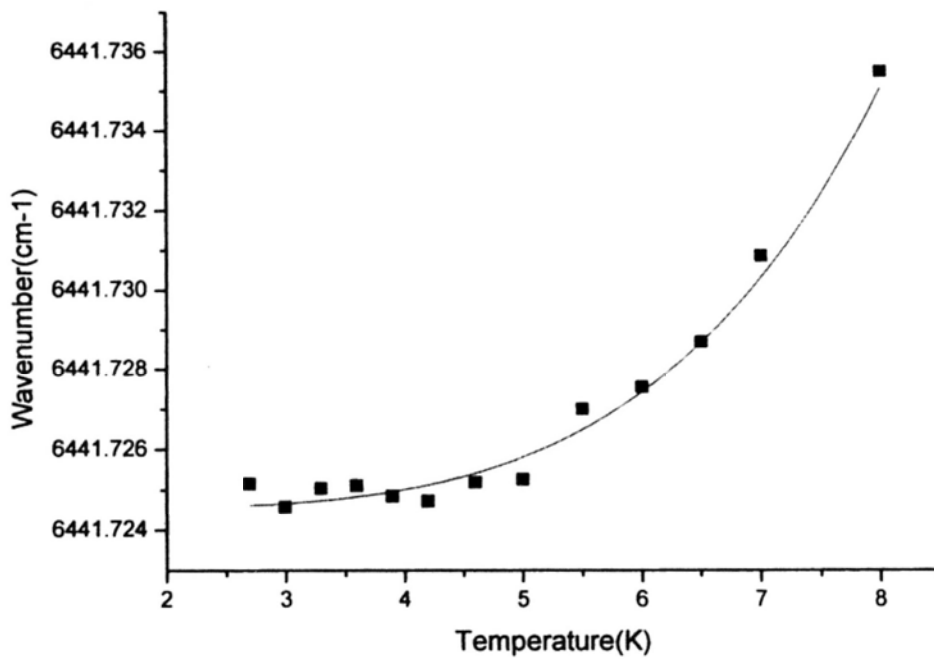


FIGURE 15 Angle-independent transition frequency  $\nu_0$  of the  $W_1(0)$  transition of solid *para*-H<sub>2</sub> as a function of temperature. The solid line shows the curve  $\nu_0(T) = 6441.7245 + 9.23 \times 10^{-7} \times T^{4.49 \pm 0.40} \text{ cm}^{-1}$ , which was obtained by least squares fitting method.

during the growth process. As a result, the homogeneous linewidth and its temperature effect are completely buried in the inhomogeneous profile to exhibit little temperature dependence. This interpretation is consistent with the observed amplitude modulated spectrum that showed a Gaussian line shape with a typical width of  $\sim 0.014 \text{ cm}^{-1}$ . The  $J = 6$  roton appears to have little effect on the shift and linewidth indicating the weakness (64-pole)-(64-pole) interaction. It will be interesting to see the temperature effect under constant molecular volume. Experiment along this line is underway.

#### IV.4. Discussion

It was seen that all three  $M$  components of  $W_1(0)$  transition were observed in crystals of  $\sim 99.95\%$  *para*- $\text{H}_2$  with both laser polarizations. The prominence of the  $|M| = 3$  transition with both laser polarizations may be explained by the fact that the crystal  $c$  axis is along the radial direction based on the geometry of the sample cell. This distortion not only gives rise to a greater  $\epsilon_{2c}$ , but also leads to a residual polarization parallel to the  $c$  axis regardless the polarization of light used in the experiments. In addition, the finite size of laser beam and the polycrystalline nature of the crystal also deviates the ideal polarization conditions required to observe a clear-cut polarization dependence of the  $M$  components.

While we have confirmed in our experiments the localized roton in the case of  $W$  transition, the role of roton in the relaxation process as well as linewidth has yet to clarify. As discussed above, the amplitude modulated transition with a Gaussian line shape and a typical width of  $\sim 0.014 \text{ cm}^{-1}$  is very likely inhomogeneous broaden due to crystal-strain generated during the growth process. It is known that the  $Q_1(0)$  transition exhibits a homogeneous width of  $\leq 5\text{MHz}$  at  $5.7 \text{ K}$ .<sup>77</sup> If the inhomogeneity

can be removed, it is likely to observe a similar linewidth for the  $W_1(0)$  transitions. If successful, the crystal field split  $M$  components may be observed without using frequency modulation technique in which the true linewidth and intensity cannot be obtained. In addition, the temperature dependence of the transition frequency, linewidth, and line shape will also be studied with high accuracy to provide the dynamic information of the  $J = 6$  rotons.

In summary, the crystal field splitting of the  $W_1(0)$  transition of solid *para*-H<sub>2</sub> was observed in crystals with 99.95%  $J = 0$  molecules using high resolution near infrared diode laser spectrometer. The corresponding crystal field parameters  $\epsilon_{2c}$  and  $\epsilon_{4c}$  together with the angle-independent transition frequency  $\nu_0$  were determined using least-squares fitting. These parameters are in good agreement with the previous studies of the  $W_0(0)$  transition to confirm the localization of  $J = 6$  rotons.<sup>25</sup> The temperature dependence of the  $W_1(0)$  transition was also studied in the temperature range of 2.7-8.0 K. The observed frequency shift was satisfactorily interpreted by molar volume change at different temperature while the linewidth studies provide no clear cut trend due to serious inhomogeneous broadening.

# CHAPTER V. Spectroscopic Study of Ammonia in Parahydrogen Matrix

## V.1. Introduction

Ammonia,  $^{14}\text{NH}_3$ , is the first polyatomic molecule observed in the interstellar space and also one of the most studied species in molecular spectroscopy.<sup>78-80</sup> It has a trigonal pyramidal shape with the nitrogen atom at the apex and the three hydrogen atoms in a triangle as a base. As shown in FIGURE 16, a planar configuration of  $\text{NH}_3$  can be obtained by the symmetric bending motion (also known as the umbrella motion) of the three hydrogens and further bending leads to a symmetrically equivalent pyramidal configuration. The two pyramidal configurations correspond to the nitrogen atom located on either side of the plane formed by the hydrogen atoms. Since the energy of the planar configuration is about  $2000\text{ cm}^{-1}$  above the pyramidal configurations, the classical pathway of symmetric bending gives a prototypical symmetric double well potential energy surface for quantum mechanical tunneling motion. As predicted in quantum mechanics, states with energy lower than the finite barrier can penetrate through the classically forbidden region to reach the other well of the potential. In other words, the wavefunctions in such a potential is delocalized. The delocalized wavefunctions can be written as the symmetric and antisymmetric combinations of the localized wavefunctions associated with the two symmetrically equivalent configurations, *i.e.*

$$\psi^{\pm} = \frac{1}{\sqrt{2}}(\psi_L \pm \psi_R)$$

(V - 1)

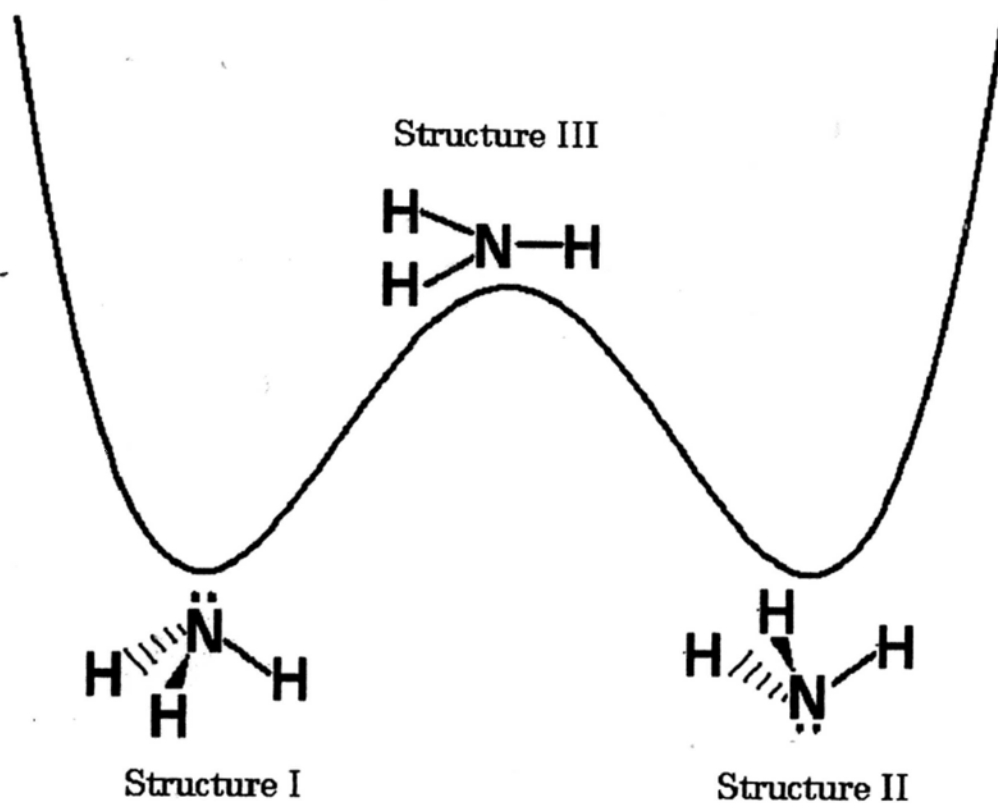


FIGURE 16. Schematic representation of the two structures for ammonia. Due to its inversion potential energy surface, NH<sub>3</sub> molecule can convert between structures I and II.

where  $\psi^+$  and  $\psi^-$  are the symmetric wavefunction and antisymmetric wavefunction, respectively. The delocalization of wavefunctions leads to splitting of energy levels, known as inversion splitting in the case of  $\text{NH}_3$ . Due to this interesting phenomenon,  $\text{NH}_3$  has been long been a subject for studying quantum mechanical tunneling. Spectroscopic study of transitions between inversion doublets was first reported in the far infra-red region by Wright and Randall.<sup>81</sup> They observed the splitting in gas phase has been found to be  $0.79 \text{ cm}^{-1}$  and  $35.7 \text{ cm}^{-1}$  in the ground vibrational state and in the  $\nu_2 = 1$  vibrational excited state, respectively.<sup>82-83</sup>

Studies of inversion tunneling of  $\text{NH}_3$  in solid matrix of nitrogen and rare gases have been carried out extensively. Early spectra of  $\text{NH}_3$  trapped in argon and nitrogen matrices revealed no complicated absorption pattern in addition to a single prominent peak in the  $\nu_2$  region which suggested the aggregated species of ammonia without molecular inversion or rotation.<sup>84-85</sup> However, subsequent studies in the  $\nu_2$  region of  $\text{NH}_3$  trapped in argon matrix exhibited several peaks resulting from the inversion and/or rotation of  $\text{NH}_3$  molecules.<sup>86-87</sup> Hereafter, the observations of  $\text{NH}_3$  impurities in various matrices, such as neon, krypton, xenon<sup>88-89</sup>, and He-droplets<sup>90</sup>, led to similar conclusions. Additional studies of the temperature and time dependence of various peaks also provided the evidences for the existence of the rotation and inversion of  $\text{NH}_3$  trapped in these matrix environments. Although the motion of  $\text{NH}_3$  in matrices are similar to those in the gas phase, the inversion splitting of the  $\nu_2$  vibrational mode in rare gas matrices is decreased by about 30% with respect to the gas phase value as a result of smaller tunneling probability due to the stronger intermolecular interactions. Recent studies of Infrared<sup>91</sup> and Raman<sup>92</sup> spectra of  $\text{NH}_3$  molecule in nitrogen matrices have also revealed the evidence of hindered rotation.

Compared to other commonly used matrix materials, solid parahydrogen appears to be a more suited matrix to studying the rovibrational and tunneling motions of  $\text{NH}_3$ . The distinctive quantum properties of solid  $\text{H}_2$  have been known to facilitate motions of embedded molecular species. Due to its weak intermolecular interactions and large intermolecular separation, it allows molecular motions with little hindrance. In fact, it has been known that small diatomic molecules (*e.g.* CO) in solid  $\text{H}_2$  exhibit rovibrational spectrum that is similar to those in gas phase.<sup>40</sup> These factors will no doubt favor the inversion tunneling of  $\text{NH}_3$  in parahydrogen matrix.

In the present work, we studied the  $\nu_2$  fundamental band of ammonia embedded in *para*- $\text{H}_2$  matrix in an attempt at investigating the inversion tunneling. The observed spectrum appeared to be very different from those observed in other matrix materials. Based on the effect of crystal annealing and nuclear spin conversion on the  $\nu_2$  band, a preliminary analysis has been done. The details of the study will be discussed in this chapter. Since the spectrum has yet to be completely understood, further work is underway.

## V.2. Theoretical Aspects

### V.2.1. Group theoretical considerations

The group theory to qualitatively analyze the spectra of  $\text{NH}_3$  in *para*- $\text{H}_2$  matrix can be established based on the framework discussed in Chapter II. Similar to the case of  $W$  transition, an *hcp* crystal environment is assumed. The central molecule under consideration is an  $\text{XY}_3$  molecule (*i.e.*  $\text{NH}_3$ ) as shown in

FIGURE 17. The crystal field is expected to lift the degeneracy of the rotational levels as well as to increase the barrier of inversion of  $\text{NH}_3$ . To classify the rotational levels of  $\text{NH}_3$  and

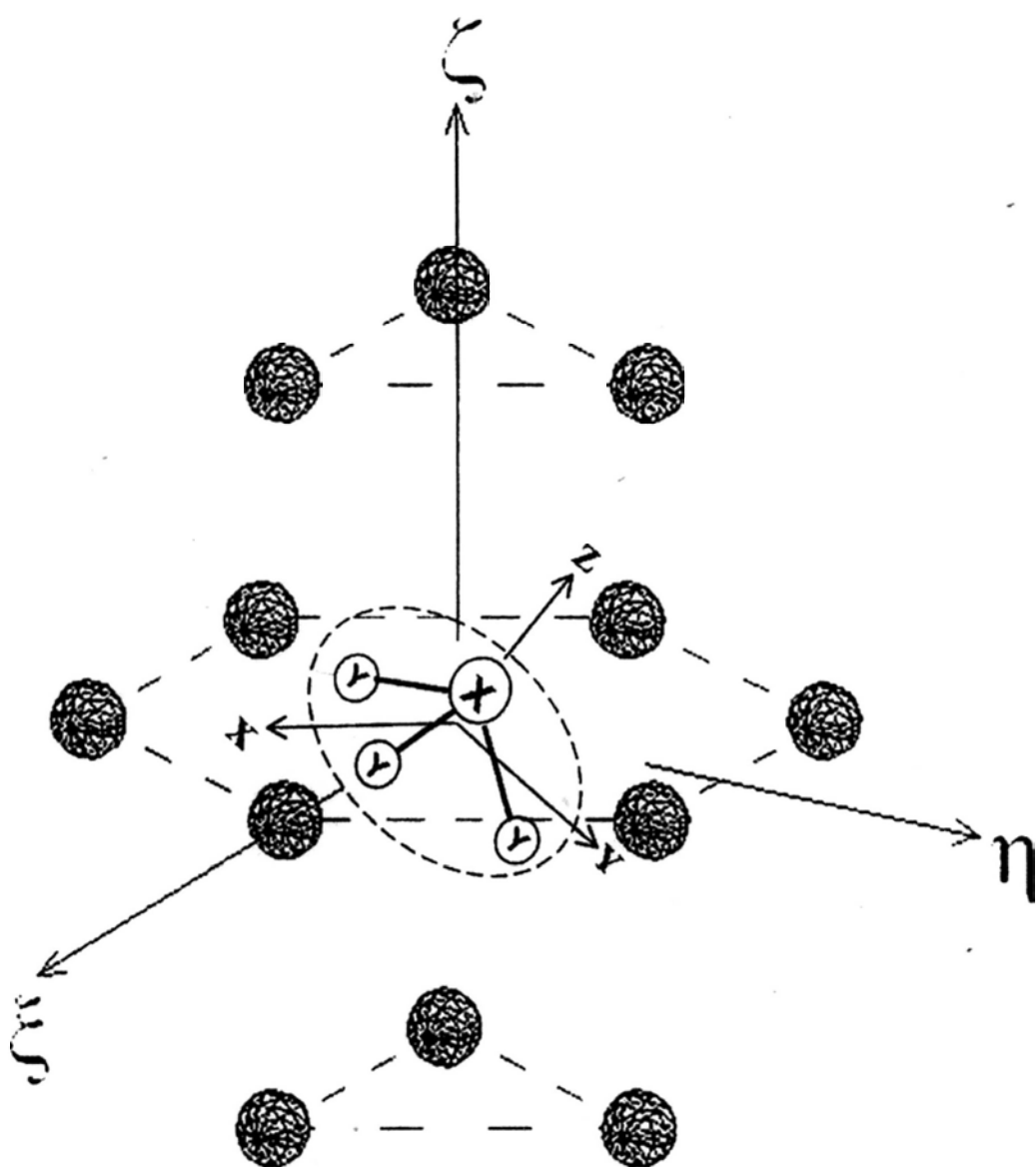


FIGURE 17 Crystal structure of an  $XY_3$  molecule trapped in the  $hcp$  crystal of  $para$ - $H_2$ . The filled circles indicate  $para$ - $H_2$  molecules and the small empty circles indicate an  $XY_3$  molecule. In the crystal-fixed axis system, the crystal  $\zeta$  axis is perpendicular to the hexagonal plane and the  $\xi$  axis is in the plane. In the molecule-fixed system, the  $C_3$  symmetry axis of the radical is taken as the  $z$  axis of the molecule  $XY_3$  and  $xy$  axis is in the plane perpendicular to the  $z$  axis.

determine the selection rules, we need to construct the appropriate extended group following the prescription of Miller and Decius.<sup>60</sup>

Taking into account the inversion tunneling, the molecular symmetry group of NH<sub>3</sub> is  $\overline{D}_{3h}$  with operations:

$$\overline{D}_{3h} = \{\overline{E}, 2\overline{(123)}, 3\overline{(23)}, \overline{E}^*, 2\overline{(123)}^*, 3\overline{(23)}^*\}, \quad (\text{V} - 2)$$

where overbar is used on the molecular symmetry group operations as before,  $\overline{E}$  and  $\overline{E}^*$  are the identity and space inversion operation, respectively,  $\overline{(23)}$  is the permutation of the two identical particles and  $\overline{(123)}$  is a cyclic permutation of identical particles. On the other hand, the point symmetry group of the *hcp* crystal is also  $D_{3h}$  with operations:

$$D_{3h} = \{E, 2C_3, 3C_2, \sigma_h, 2S_3, 3\sigma_v\}, \quad (\text{V} - 3)$$

where the  $C_3$  axis is along the  $c$  axis of the crystal (i.e. the space-fixed  $\zeta$  axis) and the symbol of each operation is written in the standard point group notation<sup>71</sup>. As discussed in Chapter II, the appropriate extended group  $G_{72}$  is constructed the following way:

$$G_{72} = \{E, 2C_3, 3C_2\} \otimes \{\overline{E}, 2\overline{(123)}, 3\overline{(23)}\} + \{\sigma_h, 2S_3, 3\sigma_v\} \otimes \{\overline{E}^*, 2\overline{(123)}^*, 3\overline{(23)}^*\} \quad (\text{V} - 4)$$

The extended group  $G_{72}$ , which is composed only 72 elements, is the subgroup of the direct product group of  $D_{3h} \otimes \overline{D}_{3h}$ . TABLE 6 shows the corresponding character table constructed using standard procedures in group theory. The symmetry classifications of the dipole moment  $\mu$  and the polarizability tensor  $\alpha$  are also listed in the table.

Using the symmetric top rotational wavefunctions, the rotational levels of NH<sub>3</sub>

are the functions of Euler angles  $\{\chi\theta\phi\}$  that define the relative orientation between the molecule-fixed axis system with respect to the crystal-fixed axis system and specified by three quantum number  $J$  (total angular momentum),  $M$  (projection of  $J$  along the crystal-fixed  $\zeta$  axis), and  $K$  (projection of  $J$  along the molecule-fixed  $z$  axis), *i.e.*:

$$|JKM\rangle = \sqrt{(2J+1)/8\pi^2} D_{KM}^{(J)}(\{\chi\theta\phi\}) \quad (\text{V - 5})$$

where the Wigner's rotation matrix  $D_{KM}^{(J)}(\{\chi\theta\phi\})$  follows the sign convention of Bunker and Jensen.<sup>93</sup> By considering the transformation properties of Euler angles  $\{\chi\theta\phi\}$  under each operator of the extended group  $G_{72}$ , their effect on rotational wavefunction  $|JKM\rangle$  follows:

$$R_{\chi\theta\phi} \overline{R_{\chi'\theta'\phi'}} |JKM\rangle = \sum_{M'} \sum_{K'} D_{M'M}^{(J)}(\chi\theta\phi) D_{KK'}^{(J)}(\chi'\theta'\phi') |J'K'M'\rangle \quad (\text{V - 6})$$

where  $\chi\theta\phi$  and  $\chi'\theta'\phi'$  stand for the change of the Euler angles corresponding to the symmetry operations in extended group  $G_{72}$  with respect to crystal and molecule, respectively, and  $R_{\chi\theta\phi} \overline{R_{\chi'\theta'\phi'}}$  represents the equivalent rotation corresponding to symmetry operation. The detailed transformation properties of Euler angles under the symmetry operations of group  $D_{3h}$  are listed in TABLE 7. By applying these transformation properties into Equation (V-6), the irreducible representation of the rotational wavefunctions using the standard projection operator method can be easily worked out. TABLE 8 shows the explicit expressions for the symmetry classifications of the rotational wavefunctions. In addition to the splitting for  $K$  sub-levels as in gas phase, the  $M$  sub-levels are no longer degenerate but split as a result of spatial anisotropy in the crystal. For instance, the  $J = 1$  is split into  $A_2 \oplus E'$  components for  $M = 0$  and  $\pm 1$ , respectively, while the  $J = 2$  state is

TABLE 6 Character table of group  $G_{72}$ .

$G_{72}$	$1E$	$2E$	$3E$	$2C_3$	$4C_3$	$6C_3$	$3C_2$	$6C_2$	$9C_2$	$1\sigma_h$	$2\sigma_h$	$3\sigma_h$	$2S_3$	$4S_3$	$6S_3$	$3\sigma_v$	$6\sigma_v$	$9\sigma_v$	
	$\bar{E}$	$\frac{(123)}{(23)}$	$\frac{3E}{(23)}$	$\frac{2C_3}{E}$	$\frac{4C_3}{(123)}$	$\frac{6C_3}{(23)}$	$\frac{3C_2}{E}$	$\frac{6C_2}{(123)}$	$\frac{9C_2}{(23)}$	$\frac{1\sigma_h}{E^*}$	$\frac{2\sigma_h}{(123)^*}$	$\frac{3\sigma_h}{(23)^*}$	$\frac{2S_3}{E^*}$	$\frac{4S_3}{(123)^*}$	$\frac{6S_3}{(23)^*}$	$\frac{3\sigma_v}{E^*}$	$\frac{6\sigma_v}{(123)^*}$	$\frac{9\sigma_v}{(23)^*}$	
$A_1A_1$	1	1	1	1	1	1	1	1	1	1	1	1	1	1	1	1	1	1	$\alpha_{ZZ}, \alpha_{XX} + \alpha_{YY}$
$A_1A_1$	1	1	1	1	1	1	1	1	1	-1	-1	-1	-1	-1	-1	-1	-1	-1	
$A_1A_2$	1	1	-1	1	1	-1	1	1	-1	1	1	-1	1	1	-1	1	1	-1	
$A_1A_2$	1	1	-1	1	1	-1	1	1	-1	-1	-1	1	-1	-1	1	-1	-1	1	
$A_1E$	2	-1	0	2	-1	0	2	-1	0	2	-1	0	2	-1	0	2	-1	0	
$A_1E$	2	-1	0	2	-1	0	2	-1	0	-2	1	0	-2	1	0	-2	1	0	
$A_2A_1$	1	1	1	1	1	-1	-1	-1	-1	1	1	1	1	1	1	-1	-1	-1	
$A_2A_1$	1	1	1	1	1	-1	-1	-1	-1	-1	-1	-1	-1	-1	-1	1	1	1	
$A_2A_2$	1	1	-1	1	1	-1	-1	-1	-1	1	1	-1	1	1	-1	-1	-1	1	$\mu_2$

(Continued)

$G_{72}$	$\frac{1E}{\bar{E}}$	$\frac{2E}{(123)}$	$\frac{3E}{(23)}$	$\frac{2C_3}{\bar{E}}$	$\frac{4C_3}{(123)}$	$\frac{6C_3}{(23)}$	$\frac{3C_2}{\bar{E}}$	$\frac{6C_2}{(123)}$	$\frac{9C_2}{(23)}$	$\frac{1\sigma_h}{\bar{E}}$	$\frac{2\sigma_h}{(123)}$	$\frac{3\sigma_h}{(23)}$	$\frac{2S_3}{\bar{E}}$	$\frac{4S_3}{(123)}$	$\frac{6S_3}{(23)}$	$\frac{3\sigma_v}{\bar{E}}$	$\frac{6\sigma_v}{(123)}$	$\frac{9\sigma_v}{(23)}$
$A_2A_2$	1	1	-1	1	1	-1	-1	-1	1	-1	-1	1	-1	-1	1	1	1	-1
$A_2E$	2	-1	0	2	-1	0	-2	1	0	2	-1	0	2	-1	0	-2	1	0
$A_2E$	2	-1	0	2	-1	0	-2	1	0	-2	1	0	-2	1	0	2	-1	0
$EA_1$	2	2	2	-1	-1	-1	0	0	0	2	2	2	-1	-1	-1	0	0	0
$EA_1$	2	2	2	-1	-1	-1	0	0	0	-2	-2	-2	1	1	1	0	0	0
$EA_2$	2	2	-2	-1	-1	1	0	0	0	2	2	-2	-1	-1	1	0	0	0
$EA_2$	2	2	-2	-1	-1	1	0	0	0	-2	-2	2	1	1	-1	0	0	0
$EE$	4	-2	0	-2	1	0	0	0	0	4	-2	0	-2	1	0	0	0	0
$EE$	4	-2	0	-2	1	0	0	0	0	-4	2	0	2	-1	0	0	0	0

$(\mu_x, \mu_y)$

$\alpha_{XY}, \alpha_{XX} - \alpha_{YY}$

$\alpha_{XZ}, \alpha_{YZ}$

TABLE 7 Values of the Euler angles  $\{\chi\theta\phi\}$  corresponding to the symmetry operations of point group  $D_{3h}$ .

Operation	$\chi$	$\theta$	$\phi$
$E$	0	0	0
$C_3(z)$	$\frac{2}{3}\pi$	0	0
$C_3^2(z)$	$\frac{4}{3}\pi$	0	0
$C_2(1)$	$\frac{2}{3}\pi$	$\pi$	0
$C_2(2)$	0	$\pi$	0
$C_2(3)$	$\frac{4}{3}\pi$	$\pi$	0
$\sigma_h$	$\pi$	0	0
$S_3(z)$	$\frac{5}{3}\pi$	0	0
$S_3^2(z)$	$\frac{1}{3}\pi$	0	0
$\sigma_v(1)$	$\frac{5}{3}\pi$	$\pi$	0
$\sigma_v(2)$	$\pi$	$\pi$	0
$\sigma_v(3)$	$\frac{1}{3}\pi$	$\pi$	0

TABLE 8 Symmetry classifications of the rotational wavefunctions  $|JKM\rangle$   
 ( $J \leq 2$ ) in group  $G_{72}$

$ JKM\rangle$	Symmetry Classification	$ JKM\rangle$	Symmetry Classification
000	$A_1A_1'$	202	$EA_1'$
100	$A_2A_2'$	210	$A_1E''$
101	$EA_2''$	211	$EE'$
110	$A_2E''$	212	$EE''$
111	$EE'$	220	$A_1E'$
200	$A_1A_1'$	221	$EE''$
201	$EA_1''$	222	$EE'$

split into  $A_1' \oplus E' \oplus E''$  corresponding to  $M = 0, \pm 1$ , and  $\pm 2$ , respectively, in the  $D_{3h}$  crystal field.

In determining the symmetry of laboratory-fixed components of the dipole moment of  $\text{NH}_3$ , the same procedure is applied. For simplicity in the discussion later, we can consider the three spherical components instead of the Cartesian components. It is known that the three spherical components are first-ranked spherical tensor operators, which behave like spherical harmonics of  $J = 1$ . Applying the same argument as before, one has

$$\Gamma(\mu_z) = A_2''; \quad (\text{V} - 7)$$

$$\Gamma(\mu_x, \mu_y) = E' \quad (\text{V} - 8)$$

Once the symmetry representations of dipole moments and rotational levels are known, it is straight forward to determine the allowed infrared transitions.

### V.2.2. Nuclear spin modifications

Similar to the hydrogen molecule, ammonia molecule with three symmetrically equivalent protons has different nuclear spin modifications depending on the relative orientations of nuclear spins of the protons. According to the quantum theory of angular momentum, the coupling of the three protons results in total nuclear spin of  $I = 3/2$  (*ortho*) and  $I = 1/2$  (*para*) species. Similar to the case of  $\text{H}_2$ , the Pauli principle requires that *ortho* species occupy the rotational states  $K = 3n$ , ( $n = 0, 1, 2, \dots$ ) while *ortho* species occupy the  $K = 3n \pm 1$  states.<sup>94,95</sup> At room temperature, the *ortho-to-para* abundance ratio of the  $\text{NH}_3$  molecule is 2:1. Unlike diatomic species whose *ortho/para* conversion is extremely slow due to parity requirement, the *ortho/para* conversion of  $\text{NH}_3$  is much faster, only on the order of days in the gas phase. In the condensed phase, the few populated levels with smaller energy

differences result in a faster rate of conversion, as pointed out by Hougen and Oka.<sup>96</sup> Because of the “fast” conversion, this ratio is expected to change at cryogenic temperature in a time scale of hours even without the present of paramagnetic species. The evidence of the nuclear spin conversion of NH<sub>3</sub> isolated in rare-gas matrices has been observed by Hopkins.<sup>97</sup> He observed time dependence of intensities in the umbrella motion of NH<sub>3</sub> in Ar matrix, and indicated that nuclear spin conversion was a powerful aid in discriminating rotational structure from structure arising from different matrix sites or agglomeration. Since the *ortho/para* conversion is catalyzed by a paramagnetic impurity, such as O<sub>2</sub>,<sup>100</sup> the addition of traces of O<sub>2</sub> should help identify species due to the *ortho* or *para* species as we will see below.

### V.3. Observation and Preliminary Analysis

While there are four infrared active bands for NH<sub>3</sub>, we only studied the  $\nu_2$  band because others are either too weak or overlap with atmospheric absorptions. The  $\nu_2$  band located in the 10  $\mu\text{m}$  region exhibit strong transitions even with 9 ppm of NH<sub>3</sub> in solid parahydrogen taken as shown in FIGURE 18. As shown in the spectrum, the most prominent absorption was observed at 968.2 cm<sup>-1</sup>(E). with five less intense absorptions at 961.4 cm<sup>-1</sup>(A), 963.1 cm<sup>-1</sup>(B), 965.5 cm<sup>-1</sup>(C), 966.1 cm<sup>-1</sup>(D) and 976.7 cm<sup>-1</sup>(F). These absorption peaks were observed with a linewidth at 0.2 cm<sup>-1</sup>, which appeared to be limited by the resolution of our spectrometer. In addition, a broad feature was observed at ~987.3 cm<sup>-1</sup> (G). The observed transitions are listed in TABLE 9.

FIGURE 19 shows a series of spectra taken during the matrix deposition process. The peak at 968.2 cm<sup>-1</sup>(E) first appeared in the spectrum, followed by the

peaks at  $961.4\text{ cm}^{-1}$ (A),  $963.1\text{ cm}^{-1}$ (B),  $965.5\text{ cm}^{-1}$ (C), and  $966.1\text{ cm}^{-1}$ (D), the doublet at  $976.7\text{ cm}^{-1}$ (F) and the broad feature at  $987.3\text{ cm}^{-1}$ (G). It was interesting to note that the relative intensity between lines (C) and (D) as well as the transitions in the doublet (F) reversed during the growth process. In addition, a weak peak at  $949.5\text{ cm}^{-1}$  appeared during the growth process but also completely disappeared after the completion of the growth.

The annealing of the samples allows the thermodynamically less favorable *hcp* crystalline to convert to more favorable *hcp* crystalline. In addition, it also allows the ortho/para  $\text{NH}_3$  to reach Boltzmann distribution at 4.8 K. Both processes will no doubt alter the relative intensity of the observed transitions. The effect of sample annealing was also studied by keeping the sample at 4.8 K for 17 hours. A series of spectra recorded during the process are shown in FIGURE 20. The intensities of peak (A), (D) and (F) decreased at the similar rate while the intensity of peak (C) decreased much faster. On the other hand, peaks (B), (E) and (G) increased in intensity.

To accelerate the ortho/para conversion of  $\text{NH}_3$  in solid *para*- $\text{H}_2$ , trace of  $\text{O}_2$  was added to the premixed gas for matrix deposition. As shown in FIGURE 21, peaks (A), (D) and (F) were much weaker in the presence of  $\text{O}_2$  while (B), (E) and (G) became stronger. This effect was more significant at higher  $\text{O}_2$  concentration.

Based on these observations, a preliminary assignment of the spectrum has been made. First of all, peak (C) at  $965.5\text{ cm}^{-1}$  was assigned to  $\text{NH}_3$  transition in the face-centered cubic (*fcc*) crystalline, which quickly converted to *hcp* upon annealing to weaken its intensity. Since infrared transitions are strictly forbidden in *fcc* crystals due to the inversion symmetry of the crystal, it is very likely that peak (C) is due to a pure vibrational transition of  $\text{NH}_3$  accompanied by a nearby orientation change of

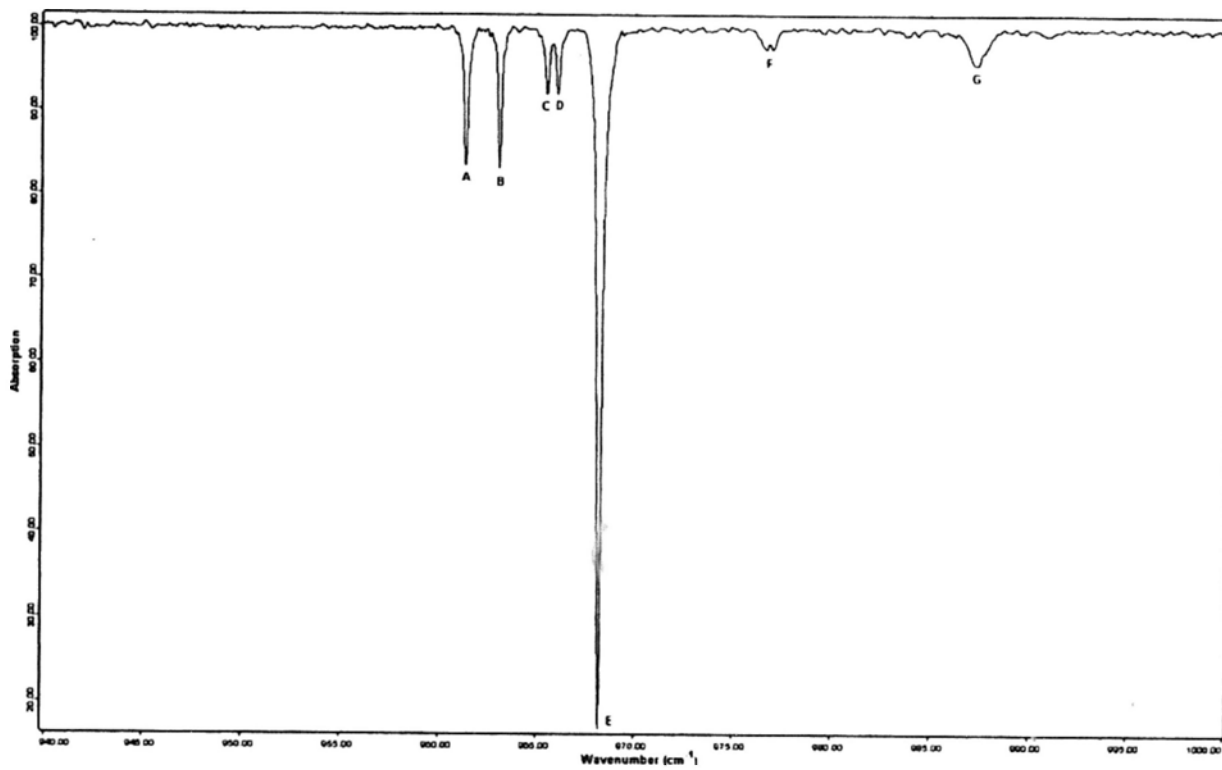


FIGURE 18 Infrared absorptions in the  $\nu_2$  region of  $\text{NH}_3$  isolated in solid *para*- $\text{H}_2$  with mole ratio of 9 ppm.

TABLE 9 Observed absorptions ( $\text{cm}^{-1}$ ) in the  $\nu_2$  region for the sample of  $\text{NH}_3$  in solid parahydrogen, with preliminary assignments.

	Frequency ( $\text{cm}^{-1}$ )	Half Width ( $\text{cm}^{-1}$ )	Assignment
	Observed	FWHM	
A	961.3540	0.23	$K = 1$
B	963.0866	0.20	$K = 0$
C	965.5258	0.23	$\text{NH}_3$ in the <i>fcc</i> $\text{H}_2$
D	966.0641	0.21	$K = 1$
E	968.2453	0.29	$K = 0$
F	976.7147*	0.26	$K = 1$
G	987.3680*	0.99	$K = 0$

(\*) Spectral lines overlapping with other lines.

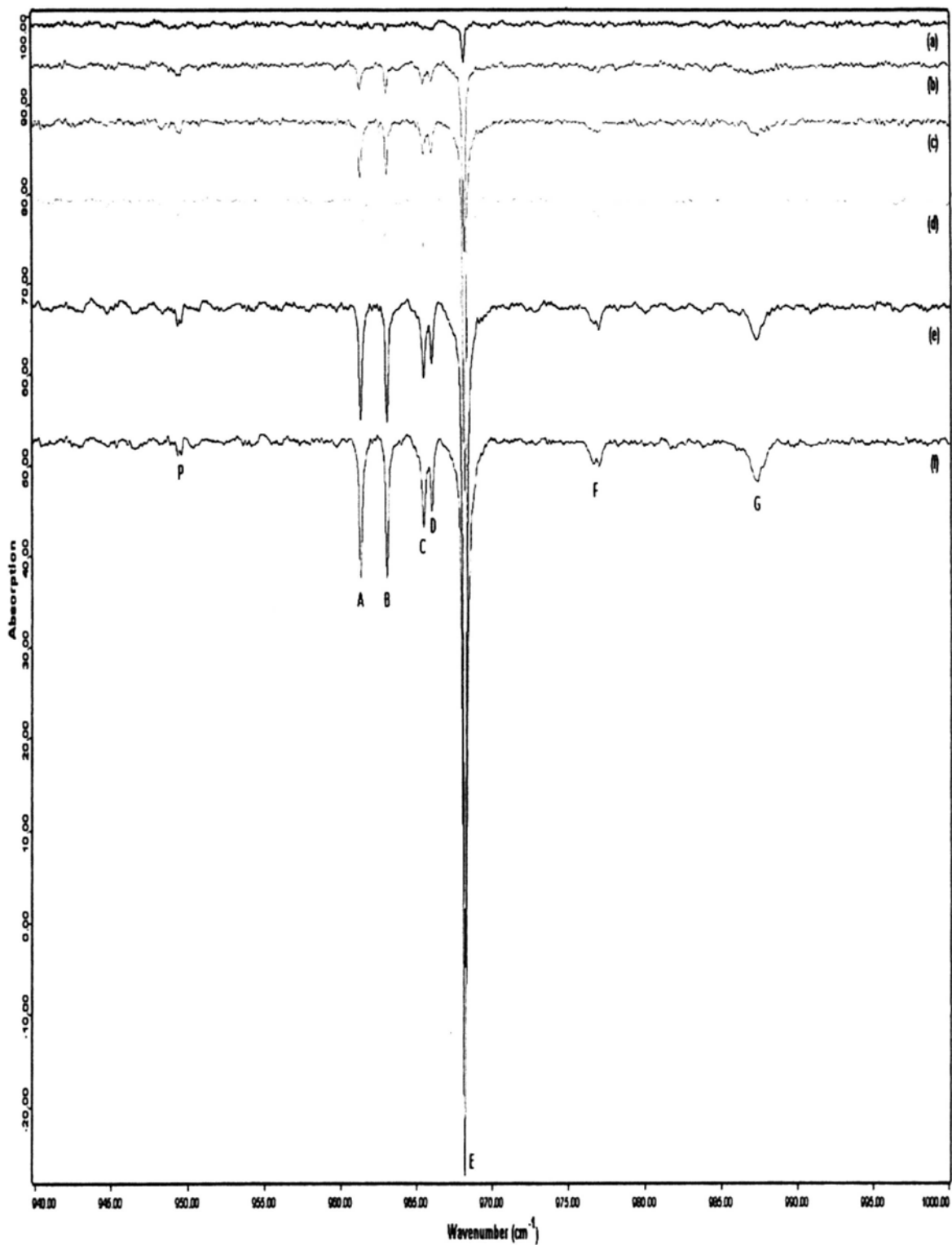


FIGURE 19 The growing process of absorption pattern in the  $\nu_2$  region of sample with 9 ppm  $\text{NH}_3$  in  $\sim 99.95\%$  *para*- $\text{H}_2$  matrix. Traces (a) to (f) show the spectra of sample at the deposition time of 8 min, 16 min, 24 min, 32 min, 40 min and 48 min, respectively.

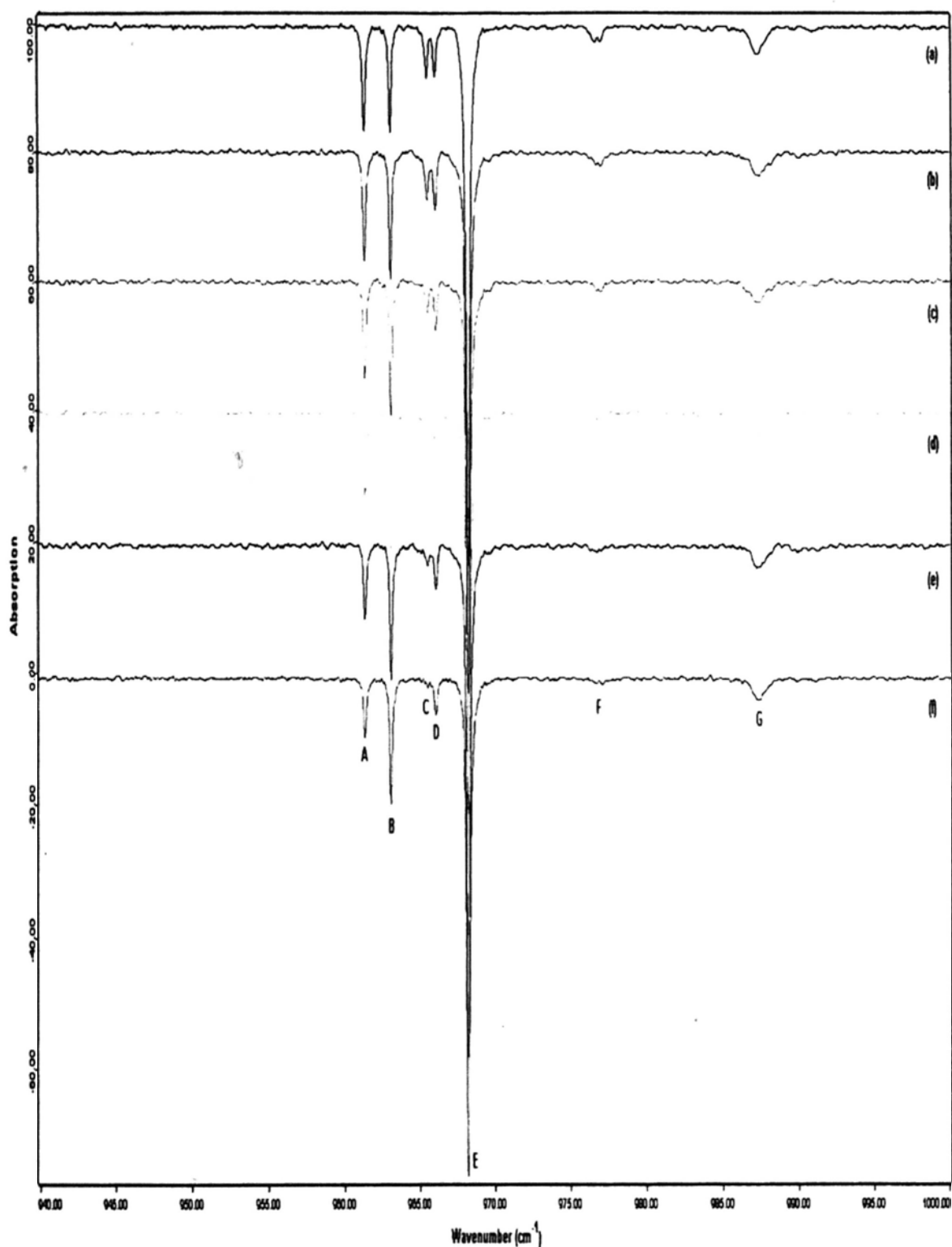


FIGURE 20 The annealing process of absorption pattern in the  $\nu_2$  region of sample with 9 ppm NH<sub>3</sub> in ~99.95% *para*-H<sub>2</sub> matrix. Traces (a) to (f) show the spectra of sample after annealing about 0 hrs, 3.5 hrs, 7.0 hrs, 10.5 hrs, 14.0 hrs, 17.5 hrs, respectively.

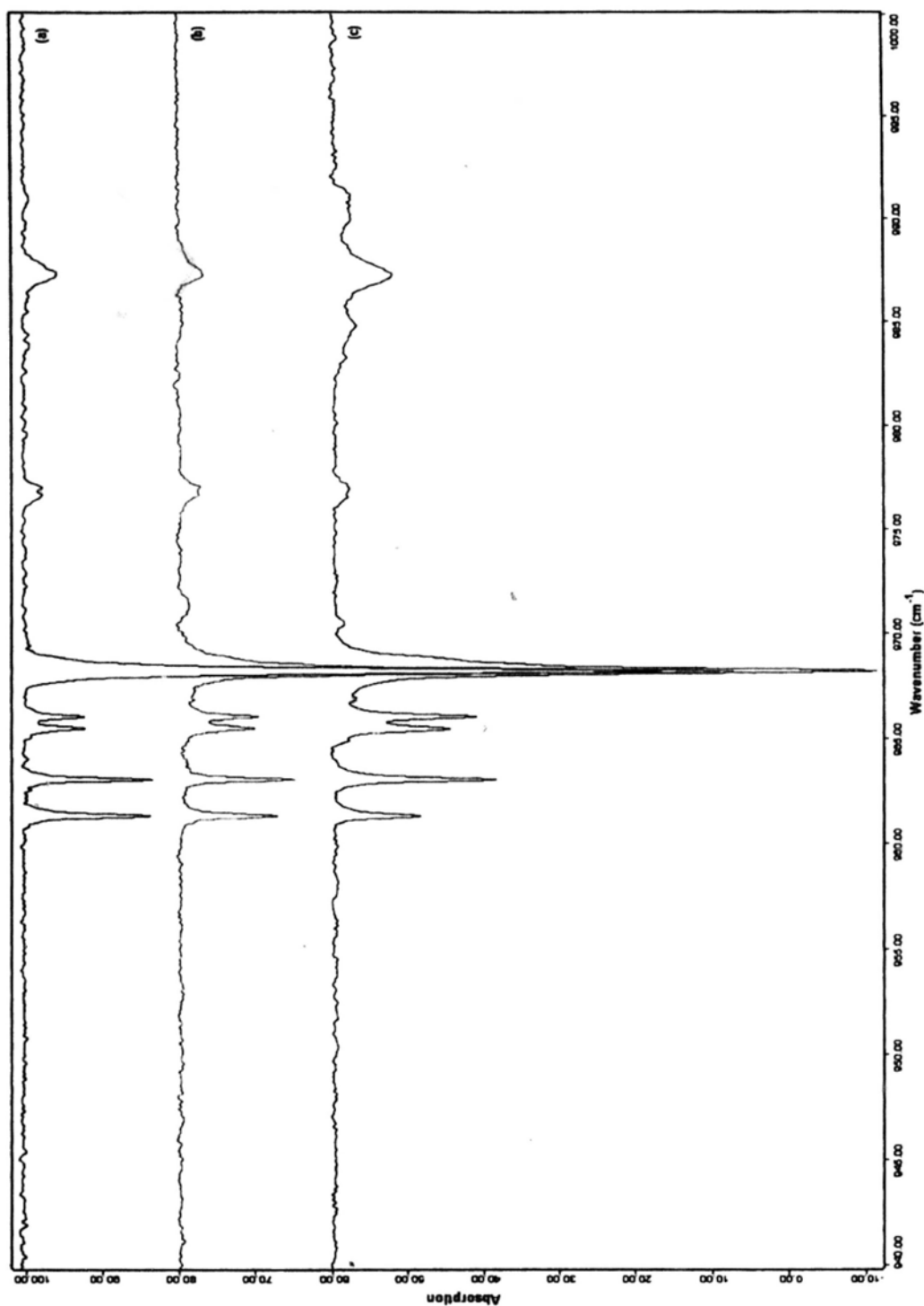


FIGURE 21 Dependence of absorption pattern on additional paramagnetic impurity  $O_2$  content in the  $\nu_2$  region of samples with 9 ppm  $NH_3$  in  $\sim 99.95\%$  *para*- $H_2$  matrix. Trace (a) shows the spectrum of sample without  $O_2$  impurity. Trace (b) shows the spectrum of sample with 110 ppm  $O_2$  impurity. Trace (c) shows the spectrum of sample with 550 ppm  $O_2$  impurity.

*ortho*-H<sub>2</sub> molecule. This configuration breaks the perfect inversion symmetry of *fcc* crystal.

Based on the change in intensities of peaks (A) at 961.4 cm<sup>-1</sup>, (D) at 966.1 cm<sup>-1</sup> and (F) at 976.7 cm<sup>-1</sup> upon annealing and in the presence of O<sub>2</sub>, these peaks were likely due to *para*-NH<sub>3</sub> species. Similarly peaks (B) at 963.1 cm<sup>-1</sup>, (E) at 968.2 cm<sup>-1</sup>, and (G) at ~987.3 cm<sup>-1</sup> were likely due to *ortho*-NH<sub>3</sub> species because of their increasing intensity upon annealing. The assignments were further confirmed by the observations in the spectra of NH<sub>3</sub> in *para*-H<sub>2</sub> matrix in the presence of O<sub>2</sub>, which would accelerate the *ortho/para* NH<sub>3</sub> conversion. Since only  $J = 0$  and 1 rotational manifolds are significantly populated at 4.8 K, the *ortho*-NH<sub>3</sub> species is expected to be  $J = 0, K = 0$  species or  $J = 1, K = 0$  species while the *para*-NH<sub>3</sub> species is expected to be  $J = 1, K = 1$  species. At this stage, the strongest absorption peak (E) appears to be due to  $J = 0, K = 0$  state judging from the strong intensity. Much more experimental work will be needed before the definite assignment of other lines can be made. Nevertheless, it is certain that NH<sub>3</sub> appears to have rovibrational motion in solid *para*-H<sub>2</sub>. It is not clear from the observed spectrum if inversion tunneling occurs.

The nature of the peak at 949.5 cm<sup>-1</sup> is not known. While peak with similar behavior in neon matrix was assigned to the  $sP(1,0)$  transitions,<sup>101</sup> its frequency, however, may not be consistent with the other transitions. At this preliminary stage, we prefer to leave it unassigned.

In summary, the  $\nu_2$  band of NH<sub>3</sub> in *para*-H<sub>2</sub> matrix exhibits sharp, lines with pattern not resemble to other matrix system. Transitions have been assigned to *ortho* and *para* species based on their behavior upon annealing and in the presence of O<sub>2</sub>. Further experiments are underway to gather more information for more definite

assignment.

## V.4. Discussion

In order to assign the transitions of the  $\nu_2$  band of  $\text{NH}_3$  in *para*- $\text{H}_2$  matrix, one may compare the corresponding spectrum of  $\text{ND}_3$ , which is known to have no tunneling in matrix. Although the nuclear spin statistics may complicate the spectrum, the identification of ortho/para species should not be difficult. With this comparison, we may be able to tell if there is inversion sub-bands for  $\text{NH}_3$ .

High resolution Raman spectroscopy may also be applicable to clarify the existence of inversion tunneling. Information complementary to infrared studies is expected because of different selection rules applied to Raman spectrum. However, the much weaker Raman spectrum posts extra difficulty and challenges. Experiments along this line are being planned.

## REFERENCE

1. H. Francis and R. Kopelman, in *Laser Spectroscopy of Solids*, edited by W. M. Yen and P. M. Selzer (Springer-Verlag, Berlin, 1986).
2. Szabo, *Phys. Rev. Lett.* **25**, 924 (1970).
3. W. E. Moerner, in *Persisted Spectral Hole Burning: Science and Application*, edited by W. E. Moerner (Springer-Verlag, New York, 1988-1989).
4. W. E. Moerner and L. Kador, *Phys. Rev. Lett.* **62**, 2535 (1989).
5. M. Orrit and J. Bernard, *Phys. Rev. Lett.* **65**, 2716 (1990).
6. E. J. Allin, W. F. J. Hare, and R. E. MacDonald, *Phys. Rev.* **98**, 554 (1955).
7. L. Pauling, *Phys. Rev.* **36**, 430 (1930).
8. W. N. Hardy and A. J. Berlinsky, *Phys. Rev. Lett.* **34**, 1520 (1975).
9. W. N. Hardy, A. J. Berlinsky, and A. B. Harris, *Can. J. Phys.* **55**, 1150 (1977).
10. A. B. Harris, A. J. Berlinsky, and W. N. Hardy, *Can. J. Phys.* **55**, 1180 (1977).
11. W. Statt, W. N. Hardy, and R. Jochemsen, *Can. J. Phys.* **58**, 1326 (1980).
12. W. Statt and W. N. Hardy, *Can. J. Phys.* **58**, 1341 (1980).
13. R. Jochemsen, B. W. Statt, and W. N. Hardy, *Can. J. Phys.* **58**, 1356 (1980).
14. M. Okumura, M. -C. Chan, and T. Oka, *Phys. Rev. Lett.* **62**, 32 (1989).
15. M. -C. Chan, M. Okumura, C. M. Gabrys, L. -W. Xu, B. D. Rehfuss, and T. Oka, *Phys. Rev. Lett.* **66**, 2060 (1991).
16. R. A. Steinhoff, K. V. S. R. Apparao, D. W. Ferguson, K. N. Rao, B. P. Winnewisser, and M. Winnewisser, *Can. J. Phys.* **72**, 1122 (1994).
17. M. -C. Chan, L. -W. Xu, C. M. Gabrys, and T. Oka, *J. Chem. Phys.* **95**, 9404 (1991).

18. D. P. Weliky, K. E. Kerr, T. J. Byers, Y. Zhang, T. Momose, and T. Oka, *J. Chem. Phys.* **105**, 4461 (1996).
19. M. -C. Chan, *Ph.D. Thesis*, (The University of Chicago, Chicago. 1991).
20. T. Momose, *J. Chem. Phys.* **107**, 7695 (1997).
21. T. Momose, M. Miki, T. Wakabayashi, T. Shida, M. -C. Chan, S. S. Lee, and T. Oka, *J. Chem. Phys.* **107**, 7707 (1997).
22. T. Momose, H. Katsuki, H. Hoshina, N. Sogoshi, T. Wakabayashi, and T. Shida, *J. Chem. Phys.* **107**, 7717 (1997).
23. M. -C. Chan, M. Okumura, and T. Oka, *J. Phys. Chem. A.* **104**, 3775 (2000)
24. T. Oka, *Phys. Rev. Lett.* **34**, 4795 (2001)
25. M. -C. Chan, S. S. Lee, M. Okumura, and T. Oka, *J. Chem. Phys.* **95**, 88 (1991).
26. P. C. Souers, *Hydrogen Properties for Fusion Energy* (University of California Press, Berkeley, 1986).
27. F. Silvera, *Rev. Mod. Phys.* **52**, 393 (1980).
28. W. H. Keesom, J. de Smedt, and H. H. Mooy, *Proc. K. Akad. Wet. Amst.* **33**, 814 (1930).
29. L. H. Nosanow, *Phys. Rev.* **146**, 120 (1966).
30. J. Van Kranendonk, *Solid Hydrogen, Theory of the Properties of Solid H<sub>2</sub>, HD, and D<sub>2</sub>*, (Plenum Press, New York. 1983).
31. E. J. Allin, T. Feldman, and H. L. Welsh, *J. Chem. Phys.* **24**, 1116 (1956).
32. H. P. Gush, W. F. J. Hare, E. J. Allin and H. L. Welsh, *Can. J. Phys.* **38**, 176 (1960)
33. R. D. G. Prasad, M. J. Clouter, and S. P. Reddy, *Phys. Rev. A.* **17**, 1690 (1978)
34. T. K. Balasubramanian, C. H. Lien, K. N. Rao and J. R. Gaines, *Phys. Rev.*

- Lett.* **47**, 1277 (1981)
35. R. A. Steinhoff, B. P. Winnewisser, and M. Winnewisser, *Phys. Rev. Lett.* **73**, 2833 (1994).
  36. T. Oka, *Ann. Rev. Phys. Chem.* **44**, 299 (1993).
  37. A. R. W. McKellar and M. J. Clouter, *Can. J. Phys.* **68**, 422 (1990)
  38. T. Momose and T. Shida, *Bull. Chem. Soc. Jpn.* **71**, 1 (1998).
  39. B. Van Zeghbroeck, *Principles of Semiconductor Devices*, (University of Colorado, Boulder, 1999)
  40. M. -C. Chan, S. S. Lee, and T. Oka (unpublished)
  41. Y. Zhang, T. J. Byers, M. -C. Chan, T. Momose, K. E. Kerr, D. P. Weliky, and T. Oka, *Phys. Rev. B.* **68**, 218 (1998).
  42. T. Momose, *J. Chem. Phys.* **107**, 7695 (1997).
  43. T. Momose, M. Miki, T. Wakabayashi, T. Shida, M. -C. Chan, S. S. Lee, and T. Oka, *J. Chem. Phys.* **107**, 7707 (1997).
  44. T. Momose, H. Katsuki, H. Hoshina, N. Sogoshi, T. Wakabayashi, and T. Shida, *J. Chem. Phys.* **107**, 7717 (1997).
  45. M. E. Fajardo and S. Tam, *J. Chem. Phys.* **108**, 4237 (1998)
  46. S. Tam and M. E. Fajardo, *J. Chem. Phys.* **111**, 4191 (1999).
  47. S. Tam and M. E. Fajardo, *Low. Temp. Phys.* **26**, 653 (2000)
  48. M. E. Fajardo and S. Tam, *J. Chem. Phys.* **115**, 6807 (2001)
  49. D. T. Anderson, R. H. hinde, S. Tam and M. E. Fajardo, *J. Chem. Phys.* **116**, 594 (2002)
  50. H. Katsuki and T. Momose, *Phys. Rev. Lett.* **84**, 3286 (2000).
  51. R. B. Scott, *Cryogenic Engineering*, (Met-Chem Research, Boulder, CO. 1959).

52. R. G. Bohn and C. F. Mate, *Phys. Rev. B.* **2**, 2121 (1970).
53. J. R. Durig, *Analytical Applications of FT-IR to Molecular and Biological Systems*, (Springer-Verlag, New York. 2004).
54. H. W. Wooley, R. B. Scott, and F. G. Brickwedde, *J. Research NBS*, **41**, 379 (1948).
55. Y. E. Stetsenko, D. N. Bol'shutkin, and L. A. Indan, *Sov. Phys. Solid State*, **12**, 2958 (1971).
56. M. Hargittai, I. Hargittai, *Symmetry through the Eyes of a Chemist*. 2nd ed. (Plenum Press, New York. 1995).
57. F. A. Cotton, *Chemical Applications of Group Theory*, 3rd ed. (Wiley, New York. 1990)
58. R. L. Carter, *Molecular Symmetry and Group Theory*, (Wiley, New York. 1998)
59. R. L. Flurry Jr., *Symmetry Groups: Theory and Chemical Applications*, (Prentice-Hall, Englewood Cliffs. 1980)
60. R. E. Miller and J. C. Decius, *J. Chem. Phys.* **59**, 4871 (1973)
61. M. E. Rose, *Elementary Theory of Angular Momenta*, (J. Wiley and Sons, Inc. New York. 1957)
62. C. -F. Yu, K. B. Whaley, C. S. Hogg, S. J. Sibener, *J. Chem. phys.* **83**, 4217 (1985).
63. A. P, Mishra, T. K. Balasubramanian, R. H. Tipping, Q. Ma, *J. Mol. Struct.* **695**, 103 (2004).
64. J. van Kranendonk, *Physica*. **25**, 1080 (1959)
65. J. van Kranendonk, *Can. J. Phys.* **38**, 240 (1960).
66. W. Ivancic, T. K. Balasubramanian, J. R. Gainer, and K. N. Rao, *J. Chem.*

- Phys.* **74**, 1508 (1981).
67. T. K. Balasubramanian, C. Lien, K. N. Rao, and E. K. Damon, *J. mol. Spectrosc.* **92**, 77 (1982).
68. See, for example, R. M. Dickson, T. Momose, T. J. Byers, T. Oka, *Phys. Rev. B.* **57**, 941(1998).
69. K. E. Kerr, T. J. Byers, B. F. Ventrudo, T. Momose, D. T. Casidy, T. Oka, in *Abstracts of the 47th Symposium on Molecular Spectroscopy*, (Columbus, Ohio, Paper RG03. 1992).
70. R. Dickson, T. Oka, *J. Phys. Chem.* **99**, 2618 (1995).
71. L. D. Landau and E. M. Lifshitz, *Quantum Mechanics: Non-Relativistic Theory*, 3rd ed, (Pergamon, New York. 1977)
72. F. Mulder, A. van der Avoird, P. E. S. Wormer, *Mol. Phys.* **37**, 157 (1979).
73. T. K. Balasubramanian, R. D'Suza, R. D'Cunha, K. Narahari Rao, *Can. J. Phys.* **67**, 79 (1989).
74. I. N. Krupskii, A. I. Prokhvatilov, and G. N. Shcherbakov, *Sov. J. Low Temp. Phys.* **9**, 42 (1983).
75. K. E. Kerr, T. Momose, D. P. Weliky, C. M. Gabrys, and T. Oka, *Phys. Rev. Lett.* **72**, 3957 (1994).
76. M. Mengel, B. P. Winnewisser, M. Winnewisser, *Phys. Rev. B.* **55**, 10420 (1997).
77. K. Kuroda, A. Koreeda, S. Takayanagi, M. Suzuki, K. Hakuta, *Phys. Rev. B.* **67**, 184303 (2003).
78. A. C. Cheung, D. M. Rank, C. H. Townes, D. D. Thornton, W. J. Welch, *Phys. Rev. Lett.* **21**, 1701 (1968)
79. C. H. Townes, A. L. Schawlow, *Microwave Spectroscopy*. (McGraw-Hill,

- New York, 1955)
80. S. G. Kukolich, *Phys. Rev.* **156**, 83 (1967)
  81. N. Wright and H. M. Randall, *Phys. Rev.* **44**, 391 (1933)
  82. I. Kleiner, L. R. Brown, G. Tarrago, Q. L. Kou, N. Picque, G. Guelachvili, V. Dana, and J. Y. Mandin, *J. Mol. Spectrosc.* **193**, 46, (1999).
  83. G. Guelachvili, A. H. Abdullah, N. Tu, K. N. Rao, S. Urban, and D. Papousek, *J. Mol. Spectrosc.* **133**, 345 (1989).
  84. D. E. Milligan, R. M. Hexter, and K. Dressler, *J. Chem. Phys.* **34**, 1009 (1961)
  85. G. C. Pimentel, M. Bulanin, and M. Van Thiel, *J. Chem. Phys.* **36**, 500 (1962)
  86. H. P. Hopkins Jr., R. F. Curl Jr., and K. S. Pitzer, *J. Chem. Phys.* **48**, 2959 (1968)
  87. L. Abouaf-Marguin, H. Dubost, and F. Legay, *Chem. Phys. Lett.* **7**, 61 (1970)
  88. L. Abouaf-Marguin, and H. Dubost, *Chem. Phys. Lett.* **15**, 445 (1972)
  89. L. Abouaf-Marguin, M. E. Jacox and D. E. Milligan, *J. Chem. Phys.* **67**, 34 (1977)
  90. M. Behrens, U. Buck, R. Frochtenicht, M. Hartmann, F. Huisken, and F. Rohmund, *J. Chem. Phys.* **109**, 5914 (1998)
  91. B. Nelander, *Chem. Phys.* **87**, 283 (1984)
  92. Loutellier, J. P. Perchard, *J. Mol. Struct.* **198**, 51 (1989)
  93. P. R. Bunker and P. Jensen, *Molecular Symmetry and Spectroscopy*, 2nd ed., (NRC Research Press, Ottawa, Ontario, Canada, 1998)
  94. E. B. Wilson Jr., *J. Chem. Phys.* **3**, 276 (1935).
  95. A. W. Maue, *Ann. Phys. (Leipzig)*. **20**, 555 (1937)
  96. J. T. Hougen and T. Oka, *Science*, **310**, 1913 (2005)

97. H. P. Hopkins, R. F. Curl, K. S. Pitzer, *J. Chem. Phys.* **48**, 2959 (1968)
98. M. Miki and T. Momose, *Low Temp. Phys.* **26**, 661 (2000)
99. Y. -P. Lee, Y. -J. Wu, R. M. Lees, L. -H. Xu, J. T. Hougen, *Science*, **311**, 365 (2006)
100. V. Shevtsov, P. Malmi, E. Ylinen, M. Punkkinen, *Phys. B.* **284**, 385 (2000).
101. M. E. Jacox and W. E. Thompson, *J. Mol. Spectrosc.* **228**, 414 (2004).